



Calhoun: The NPS Institutional Archive
DSpace Repository

Theses and Dissertations

1. Thesis and Dissertation Collection, all items

2008-09

Detection of frequency hopped signals timing information using the temporal correlation function

Cheng, Yuan-Pin.

Monterey California. Naval Postgraduate School

<http://hdl.handle.net/10945/3943>

Downloaded from NPS Archive: Calhoun



Calhoun is the Naval Postgraduate School's public access digital repository for research materials and institutional publications created by the NPS community. Calhoun is named for Professor of Mathematics Guy K. Calhoun, NPS's first appointed -- and published -- scholarly author.

Dudley Knox Library / Naval Postgraduate School
411 Dyer Road / 1 University Circle
Monterey, California USA 93943

<http://www.nps.edu/library>



NAVAL POSTGRADUATE SCHOOL

MONTEREY, CALIFORNIA

THESIS

**DETECTION OF FREQUENCY HOPPED SIGNALS
TIMING INFORMATION USING THE TEMPORAL
CORRELATION FUNCTION**

by

Yuan-Pin Cheng

September 2008

Thesis Advisor:
Second Reader:

Monique P.Fargues
Roberto Cristi

Approved for public release; distribution is unlimited

THIS PAGE INTENTIONALLY LEFT BLANK

REPORT DOCUMENTATION PAGE			<i>Form Approved OMB No. 0704-0188</i>	
Public reporting burden for this collection of information is estimated to average 1 hour per response, including the time for reviewing instruction, searching existing data sources, gathering and maintaining the data needed, and completing and reviewing the collection of information. Send comments regarding this burden estimate or any other aspect of this collection of information, including suggestions for reducing this burden, to Washington headquarters Services, Directorate for Information Operations and Reports, 1215 Jefferson Davis Highway, Suite 1204, Arlington, VA 22202-4302, and to the Office of Management and Budget, Paperwork Reduction Project (0704-0188) Washington DC 20503.				
1. AGENCY USE ONLY (Leave blank)		2. REPORT DATE September 2008	1. AGENCY USE ONLY (Leave blank)	
4. TITLE AND SUBTITLE Detection Of Frequency Hopped Signals Timing Information Using The Temporal Correlation Function			5. FUNDING NUMBERS	
6. AUTHOR(S) Yuan-Pin Cheng				
7. PERFORMING ORGANIZATION NAME(S) AND ADDRESS(ES) Naval Postgraduate School Monterey, CA 93943-5000			8. PERFORMING ORGANIZATION REPORT NUMBER	
9. SPONSORING /MONITORING AGENCY NAME(S) AND ADDRESS(ES) N/A			10. SPONSORING/MONITORING AGENCY REPORT NUMBER	
11. SUPPLEMENTARY NOTES The views expressed in this thesis are those of the author and do not reflect the official policy or position of the Department of Defense or the U.S. Government.				
12a. DISTRIBUTION / AVAILABILITY STATEMENT Approved for public release; distribution is unlimited			12b. DISTRIBUTION CODE	
13. ABSTRACT (maximum 200 words) <p>This work extends earlier work derived by Overdyk and investigates the use of wavelet transform and image processing tools to estimate hopping times occurring in frequency hopping schemes. The detection algorithm identifies frequency hopping time locations found in FH schemes from the information provided by the two-dimensional short-term signal temporal correlation function. Hopping time locations are shown to be provided by identifying TCF phase discontinuities. The detection scheme has three main stages: 1. Derive the analytic version of the FH signal and compute the resulting TCF function; 2. Enhance discontinuities via the one-dimensional Wavelet transform; 3. Apply morphological image processing operations and the Hough transform to estimate hopping time locations.</p> <p>Results show that for FH signals imbedded in additive White Gaussian noise, reliable detection performance may be obtained for SNR levels above 3 dB and good detection performance for SNR levels above 6dB for 5% to 20% detection accuracy.</p>				
14. SUBJECT TERMS Frequency Hopping Signals, Wavelet Transforms, Temporal Correlation Function, Edge Detection, , Hough Transform			15. NUMBER OF PAGES 99	
			16. PRICE CODE	
17. SECURITY CLASSIFICATION OF REPORT Unclassified	18. SECURITY CLASSIFICATION OF THIS PAGE Unclassified	17. SECURITY CLASSIFICATION OF REPORT Unclassified	18. SECURITY CLASSIFICATION OF THIS PAGE UU	

NSN 7540-01-280-5500

Standard Form 298 (Rev. 8-98)
Prescribed by ANSI Std. Z39.18

THIS PAGE INTENTIONALLY LEFT BLANK

Approved for public release; distribution is unlimited

**DETECTION OF FREQUENCY HOPPED SIGNALS TIMING INFORMATION
USING THE TEMPORAL CORRELATION FUNCTION**

Yuan-Pin Cheng
Captain, Taiwan R.O.C. Army
B.S., Chung Cheng Institute of Technology, Taiwan R.O.C., 2000

Submitted in partial fulfillment of the
requirements for the degree of

MASTER OF SCIENCE IN ELECTRICAL ENGINEERING

from the

**NAVAL POSTGRADUATE SCHOOL
September 2008**

Author: Yuan-Pin Cheng

Approved by: Monique P. Fargues
Thesis Advisor

Roberto Cristi
Second Reader

Jeffrey B. Knorr
Chairman
Department of Electrical and Computer Engineering

THIS PAGE INTENTIONALLY LEFT BLANK

ABSTRACT

This work extends earlier work derived by Overdyk and investigates the use of wavelet transform and image processing tools to estimate hopping times occurring in frequency hopping schemes. The detection algorithm identifies frequency hopping time locations found in FH schemes from the information provided by the two-dimensional short-term signal temporal correlation function. Hopping time locations are shown to be provided by indentifying TCF phase discontinuities. The detection scheme has three main stages: 1. Derive the analytic version of the FH signal and compute the resulting TCF function; 2. Enhance discontinuities via the one-dimensional Wavelet transform; 3. Apply morphological image processing operations and the Hough transform to estimate hopping time locations.

Results show that for FH signals imbedded in additive White Gaussian noise, reliable detection performance may be obtained for SNR levels above 3 dB and good detection performance for SNR levels above 6dB for 5% to 20% detection accuracy.

THIS PAGE INTENTIONALLY LEFT BLANK

TABLE OF CONTENTS

I.	INTRODUCTION.....	1
II.	TEMPORAL CORRELATION FUNCTION (TCF)	5
A.	INTRODUCTION.....	5
B.	TCF DEFINITION	5
III.	DETECTING IMPROVEMENT TECHNIQUES	9
A.	PHASE UNWRAPPING FUNCTION.....	9
B.	DIFFERENTIATION	11
C.	MEDIAN FILTER.....	13
D.	NO-HOP SIGNAL CASE: SHORT-TERM VARIANCE TRACKING DECISION SCHEME.....	14
IV.	WAVELET TRANSFORM.....	19
A.	INTRODUCTION.....	19
B.	CONTINUOUS WAVELET TRANSFORM (CWT).....	20
C.	DISCRETE WAVELET TRANSFORM	23
D.	WAVELET ANALYSIS EXAMPLE.....	25
1.	DWT Analysis.....	25
2.	CWT Analysis.....	26
V.	IMAGE DETECTION AND ANALYSIS	29
A.	EDGE DETECTION.....	29
1.	First Order Gradient	30
2.	Sobel Operator	30
B.	IMAGE MORPHOLOGICAL OPERATIONS.....	31
1.	Dilation	32
2.	Erosion	33
C.	HOUGH TRANSFORM	37
VI.	DETECTION ALGORITHM AND SIMULATIONS	41
A.	DETECTION ALGORITHM	41
1.	TCF Phase Term Generation.....	42
a.	<i>FH Signal Generation.....</i>	42
b.	<i>Signal Hilbert Transformation.....</i>	47
c.	<i>Temporal Correlation Function (TCF) Generation....</i>	47
d.	<i>TCF Phase Extraction</i>	47
2.	TCF Phase Region Edges Enhancement.....	48
a.	<i>TCF Phase Term Unwrapping Along the Time Axis t.....</i>	48
b.	<i>Applying Median Filtering to the Unwrapped TCF Phase Along the Time Axis t (filter length 15).....</i>	49
c.	<i>Differentiating the Unwrap TCF Phase Along the Time Axis t.....</i>	49

d.	<i>Applying Median Filtering to the Differentiated Phase Along the Time Axis t (filter length 30)</i>	50
e.	<i>Computing the Wavelet Transform Along the Time Axis t</i>	51
f.	<i>Removing TCF Boundary Edges</i>	52
g.	<i>Threshold Wavelet Coefficients</i>	53
3.	Binary Image Processing and Estimation	53
a.	<i>Edge Detection Operation</i>	54
b.	<i>Erosion Operation Using a Diagonal Alignment Mask</i>	54
c.	<i>Hopping Time Index Estimation Using the Hough Transform</i>	55
B.	SIMULATION RESULTS	57
1.	Signal Generation Specifics	57
a.	<i>One-Hop FH Signal Case</i>	57
b.	<i>No-Hop Signal Case</i>	58
c.	<i>Pulse Shaped FH Signal</i>	58
2.	Performance Results	58
a.	<i>Detection Accuracy Performance Results</i>	58
b.	<i>Median Filter Length</i>	60
c.	<i>Pulse Shaped FH Signal</i>	62
d.	<i>No-Hop Signal Decision Using TCF Phase Variance Information</i>	64
e.	<i>Morphological Erosion Step</i>	66
f.	<i>Morphological Dilation Step After Erosion Operation</i>	70
g.	<i>Continuous Wavelet Transform (CWT) vs. Discrete Wavelet Transform (DWT) Performance</i>	72
VII.	CONCLUSIONS AND RECOMMENDATIONS	75
A.	CONCLUSIONS	75
B.	RECOMMENDATIONS	76
	LIST OF REFERENCES	79
	INITIAL DISTRIBUTION LIST	81

LIST OF FIGURES

Figure 1.	Frequency Hopped Signal, Twenty Frequency Hops, Sampling Frequency Equal to 250 Hz.	2
Figure 2.	TCF Angle of a Non-stationary Analytic Frequency Hopping Signal; Hopping Time Location at $t=150$	7
Figure 3.	Overall FH Signal Hopping Time Estimation Process; Flow Chart and Intermediary Representative Results for Each Stage.	8
Figure 4.	Unwrapping Function Impact on the TCF Phase Function; Hopping Time Location at $t=125$; Noise-Free Signal Case.	10
Figure 5.	Unwrapped TCF Phase Term at Lag $\tau=25$, SNR=9 dB.	11
Figure 6.	Unwrapped TCF Phase Term; Differentiation Step Applied to the Unwrapped TCF Phase Along the Time Axis, τ Fixed.	12
Figure 7.	Median Filter Impact on Pulse-Like Signal; Top Plot: Original Signal, Bottom Plot: Median Filter Output with Median Filter of Length 30.	14
Figure 8.	Impact Due to Successive Operations Applied to the TCF Phase for the No-hop Signal Case, $TCF(t, \tau)$ for $\tau=25$ Fixed, SNR=12dB: First median Length=15, Second Median Length=30; (a) Original TCF Phase, (b) After Phase Unwrapping, (c) After Median Filtering, (d) After Differentiating, (e) & (f) After Second Median Filter.	15
Figure 9.	$TCF(t, \tau)$ Phase Plot for Lag $\tau=25$; SNR=9dB; Top Plot: One-hop Signal Case, and Bottom Plot: No-hop Signal Case.	16
Figure 10.	Probability of Correct Detection Using the TCF Phase Short-term Variance Thresholding Scheme; No-hop Scenarios Only, Random Frequency, 250 Experiments, SNR Level Between -6 to 21 dB.	18
Figure 11.	STFT and Wavelet Analysis Time and Frequency Resolution Plot, (a) STFT Frequency vs. Time 2-D plot, (b) Wavelet Analysis Scale vs. Time 2-D plot, (c) STFT Window Examples, (d) CWT Window Examples. [After 6, 7].	20
Figure 12.	Daubechies Wavelets of Various Orders. Wavelet Highpass Function (blue continuous line), Wavelet Lowpass Function (green dash line).	22
Figure 13.	Daubechies Wavelet Analysis Filter Frequency Response, (a) Decomposition LPF Response, (b) Decomposition HPF Response.	23
Figure 14.	Wavelet Decomposition Filter Bank, (a) STFT Filter Bank, (b) Wavelet Transform Filter Bank, (c) Wavelet Transform Decomposition Tree. [After 5, 8].	24
Figure 15.	Application of the DWT to the Processed TCF Phase for a Fixed Lag Value τ ; (a) TCF Function for a Fixed Lag Value (b) Detail Coefficients, One-Level DWT Transform of (a), Haar Wavelet, (c) Detail Coefficients after Up-sampling by 2, (d) Approximation Coefficients, One-Level DWT Transform of (a).	26
Figure 16.	Application of the CWT to the Processed TCF Phase shown in Figure 15(a), (Haar Wavelet); (a) Coefficients for Scale=1, (b)	

	Coefficients for Scale =5, (c) Coefficients for Scale =9, (d) Coefficients for Scale =13, (f) Coefficients for Scale =17.	27
Figure 17.	Edge Detection Using the Sobel Method, Operator Window Size Equal to 3.	31
Figure 18.	Desired Image Shape and Resulting Potential Image Obtained after Basic Edge Detection Stage [After 10].	32
Figure 19.	The Logical Operation of Dilation and Erosion [After 10].	33
Figure 20.	Morphological Operation; 2-bit Landscape Alignment Mask [After 10].	34
Figure 21.	Dilation Operation Impact; 3-bit Radius Mask.	35
Figure 22.	Erosion Mask Orientation Impact, before and after Mask Application; 3-bit Erosion Mask with -45° Orientation.	36
Figure 23.	Erosion Operation of the Edge Detected TCF Phase Term with 3-bit Erosion Mask. (a) After 45° Mask Erosion; (b) After -45° Mask Erosion; (c) Original Plot; (d) Final Plot: Summation of (a) and (b).	37
Figure 24.	Hough Transform and Hough Line Equation [After 11].	38
Figure 25.	Overall FH Signal Timing Information Detection Algorithm Flow Chart.	41
Figure 26.	One-Hop FH Signal. (a) Basic FH Signal (no pulse shaping). (b) FH Signal with Sine Pulse-Shaping. (c) Basic FH Signal, SNR=3 dB.	43
Figure 27.	No-Hop FH signal. Basic FH Signal (no pulse shaping). (b) FH Signal with Sine Pulse Shaping. (c) Basic FH Signal, SNR=3dB.	44
Figure 28.	Frequency Response of Basic FH Signal vs. Sine Pulse-Shaped FH Signal.	46
Figure 29.	TCF Phase Plot with SNR=9 dB.	48
Figure 30.	Differentiation Operation Applied to Unwrapped TCF Phase.	50
Figure 31.	Median Filtering of the Differentiated TCF Phase Along the Time Axis t, Median Filter Length Equal to 30.	51
Figure 32.	DWT Detail Coefficients Obtained after Applying the One-Level DWT Transform (Haar wavelets) to the TCF Phase Shown in Figure 31.	52
Figure 33.	Figure 32 after Thresholding DWT Coefficients; Threshold Equal to 40% of the Coefficient with Largest Magnitude.	53
Figure 34.	2-bit Mask Erosion Operations with 45° and -45° Orientations.	55
Figure 35.	Hough Transform Plot with 6 Peaks.	56
Figure 36.	One-Hop Detection Performance Results for Different Accuracy Tolerance Levels, SNR Levels between -6db to 21dB, Frame Size=256.	60
Figure 37.	One-Hop Correct Detection Performance Results as a Function of the Median Filter Lengths; wd1: 1 st Median Filter Length, wd2: 2 nd Median Filter Length, 500 Trials per Simulation, SNR Levels Between -6dB to 21dB, 20% Tolerance Level.	61
Figure 38.	No-Hop Correct Detection Performance Results as a Function of the Median Filter Lengths; wd1: 1 st Median Filter Length, wd2: 2 nd	

	Median Filter Length, 500 Trials per Simulation, SNR Levels Between -6dB to 21dB, 20% Tolerance Level.	62
Figure 39.	One-Hop Detection Performance Results for Basic FH Signal and Half Sine Wave Pulse Shaped FH Signal; 20% Tolerance Level, SNR Levels Between -6db to 21dB, Frame Size=256.	63
Figure 40.	No-Hop Detection Performance Results for Basic FH Signal and Half Sine Wave Pulse Shaped FH Signal; 20% Tolerance Level, SNR Levels between -6db to 21dB, Frame Size=256.	64
Figure 41.	No-Hop Signal Estimation. (a) Basic No-Hop Decision (Blue Square), (b). Variance Tracking Added in Stage 1 Followed by No-Hop Decision (Green Dot), (c) Variance Tracking (Red Diamond).	65
Figure 42.	One-Hop Signal Estimation; (a) Basic One-Hop Estimation with 2-bit Erosion Mask (Blue Diamond), (b). Variance Tracking Added in Stage 1 Followed by One-Hop Estimation (Green Star), 20% Detection Tolerance Level.	66
Figure 43.	One-Hop Signal Estimation; (a) Basic One-Hop Estimation with 2-bit Erosion Mask (Blue Diamond), (b). Binary Thresholded Wavelet Transform Directly Applied to Hough Transform (Green Star).	67
Figure 44.	No-Hop Signal Estimation; (a) Basic One-Hop Estimation with 2-bit Erosion Mask (Blue Diamond), (b). Binary Thresholded Wavelet Coefficient before Hough Estimation (Green Star).	68
Figure 45.	One-Hop Estimation Algorithm for Different Erosion Mask Lengths, (a) No Erosion Mask (Blue Dot), (b) 2-bit Erosion Mask (Green Square), (c) 3-bit Erosion Mask (Red Triangle).	69
Figure 46.	No-Hop Estimation Algorithm for Different Erosion Mask Lengths, (a) No Erosion Mask (Blue Dot), (b) 2-bit Erosion Mask (Green Square), (c) 3-bit Erosion Mask (Red Triangle).	70
Figure 47.	One-Hop Detection Performances for Various Combinations of Erosion and Dilation Masks, 2 and 3-bit Erosion Masks, 20% Hopping Time Tolerance Level.	71
Figure 48.	No-Hop Detection Performances for Various Combinations of Erosion and Dilation Masks, 2 and 3-bit Erosion Masks, 20% Hopping Time Tolerance Level.	72
Figure 49.	One-Hop Detection Performances for CWT at Different Scale Values and One-level DWT Transform, 2-bit Erosion Mask, 20% Detection Tolerance Level.	73
Figure 50.	No-Hop Detection Performances for CWT at Different Scales and One-level DWT Transform, 2-bit Erosion Mask, 20% Detection Tolerance Level.	74

THIS PAGE INTENTIONALLY LEFT BLANK

LIST OF TABLES

Table 1.	TCF Phase Short-Term Variances Computed within the Estimation Frame; 10 Non-Overlapping Sub-Windows; One-Hop and No-Hop Cases.	17
Table 2.	Hopping Time Evaluation Process Using Hough Transform Parameters.	56

THIS PAGE INTENTIONALLY LEFT BLANK

EXECUTIVE SUMMARY

This work extends earlier work derived by Overdyk and investigates the use of wavelet transform and image processing tools to estimate hopping times occurring in frequency hopping schemes. The detection algorithm identifies frequency hopping time locations found in FH schemes from the information provided by the two-dimensional short-term signal temporal correlation function(TCF).

Several operations are applied to the TCF phase to emphasize hopping time occurrences, which are contained in the TCF phase discontinuities. First, we unwrap the TCF phase and apply median filtering to the unwrapped TCF phase along the time axis t . Second, we differentiate the unwrapped TCF phase along the time axis t , and apply a second median filter to the differentiated phase along the time axis t . Next, we apply the Wavelet transform to isolate the hopping time information. Finally, we follow an image processing approach to extract the hopping time information; we first apply an edge detection algorithm to extract the TCF phase region boundaries from the wavelet transformed TCF phase. Next, we apply two erosion steps with diagonal masks, one with $+45^\circ$ and the second one with -45° orientations, to remove noisy contributions. Finally we apply the Hough transform to estimate the hopping time information and discard lines not located close enough to $\pm 45^\circ$ orientations.

Simulations are conducted for one-hop and no-hop signal configurations with signals distorted by additive white Gaussian noise in SNR levels between -3 dB and 21dB for basic FH and pulse-shaped FH signals. Results show reliable detection performance may be obtained for SNR levels above 3 dB and good detection performance for SNR levels above 6dB for 5% to 20% detection accuracy.

Simulations show that the erosion step improves the probability of correct detection (PCD) by 12% when the SNR level is equal to 3 dB. However, the erosion operation does not result in consistent significant improvements overall.

Results show that the basic one-hop detection scheme reaches 100% accuracy for 5% tolerance level for SNR levels above 6dB. Results also show that no-hop decision results reach 100% for SNR levels above 6 dB.

Finally, results show that lower detection performances are obtained when half sine pulse-shaping is applied to the symbols. This is to be expected as pulse-shaping results in dampening the signal amplitude at both ends of a symbol, thereby making it harder to extract TCF phase discontinuities.

I. INTRODUCTION

Frequency hopping (FH) signal schemes are widely used today in communication applications as they are well suited for transmission in the presence of distortions and jamming. FH is a technique in which the carrier frequency jumps following a pre-determined hopping pattern (HP) only known by transmitter and receiver sides. Hopping patterns contain two essential pieces of information: when frequency changes occur, and which frequencies are used. Hopping patterns are recorded and analyzed at the receiver side to recover the information message [1]. Using a Fourier transform approach to analyze a FH signal may not be well suited to recover the specific frequency contained in the FH signal when hopping time jitter is present, as estimated hopping time information may get degraded. A significant amount of research has been conducted to identify FH patterns over the years. For example, in 1993 Hampton proposed a scheme that detects signal dwelling time edges by tracking short-term power variations for FH schemes with signal gaps at frequency switching instants [2]. This work introduced the idea that signal discontinuities occurring between two frequencies symbols is an important feature. In 1997, Overdyk investigated the use of the two-dimensional temporal correlation function to detect frequency hopping time locations occurring in frequency hopped (FH) schemes [3].

Recall that *Frequency Hopping (FH) schemes* are designed to transmit digital information in which binary data bits are grouped into blocks of a fixed size, and each block is represented by a unique carrier frequency, called a *symbol*, to be sent across the channel [4]. Thus, a FH signal is represented by a succession of narrowband tones with different frequencies $f = f_0, f_0 + \Delta f_i, i=1, \dots, N$ where Δf_i is defined as a uniform random variable in the range $[0, B_{mss}]$, B_{mss} is the available bandwidth, and N is the number of available frequency hops.

Figure 1 presents a FH signal with twenty frequency hops, where the signal frequencies are statistically uncorrelated and uniformly distributed over the bandwidth $B_{mss}=80$ Hz.

Overdyk focused on one-dimensional processing schemes and investigated the use of one-dimensional wavelet transforms in the detection task, even though the TCF Phase is a two-dimensional quantity. This thesis extends the previous work by taking advantage of the TCF two-dimensional definition and applying image processing and morphological operations to detect the frequency hopping times.

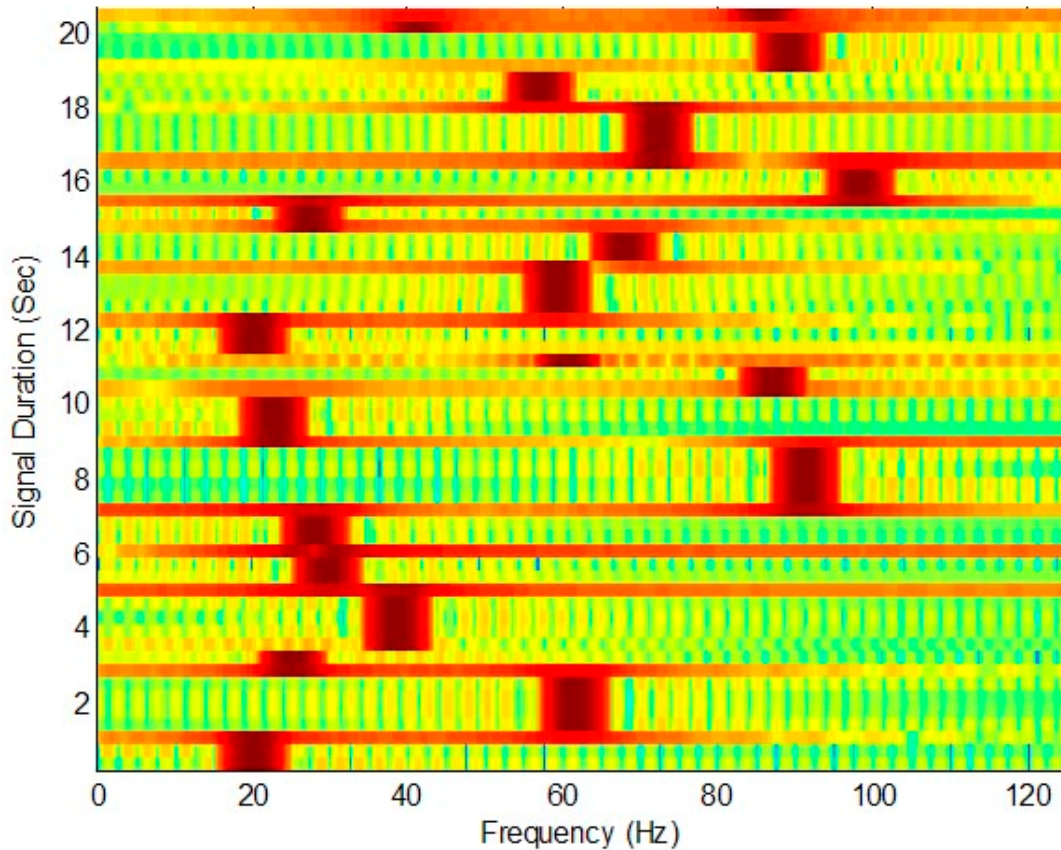


Figure 1. Frequency Hopped Signal, Twenty Frequency Hops, Sampling Frequency Equal to 250 Hz.

The thesis is composed of seven chapters including this introduction. Chapter II introduces the concept of the Temporal Correlation Function (TCF) and its application to non-stationary signals. Chapter II also discusses how to extract hopping times from the discontinuities present in the 2-dimensional TCF phase. Chapter III introduces the pre-processing techniques considered to enhance the hopping time information obtained from the TCF information. Chapter IV briefly introduces the wavelet transform and its application to high frequency signal extraction. Chapter V introduces the image morphological operations considered in this work and the Hough transform applied to the problem. Next, Chapter VI presents the overall detection algorithm implemented and resulting detection performance results obtained. Finally, Chapter VII provides conclusions and recommendations for further research.

THIS PAGE INTENTIONALLY LEFT BLANK

II. TEMPORAL CORRELATION FUNCTION (TCF)

This section introduces the concept of the temporal correlation function (TCF) and its application to the detection of frequency hopping times found in frequency hopping schemes.

A. INTRODUCTION

The temporal correlation function (TCF) of a signal $x(t)$ is defined as [3, pp. 47]:

$$TCF_x(t, \tau) = x\left(t + \frac{\tau}{2}\right) \cdot x^*\left(t + \frac{\tau}{2}\right), \quad (2.1)$$

where t is the signal time index and τ is the lag time index of the signal. The phase of the TCF matrix was used previously in Overdyk in conjunction with the one-dimensional wavelet transform [3, pp. 47-51] to extract frequency hopping time locations. The TCF is used again in this thesis in the first phase of the detection algorithm.

B. TCF DEFINITION

Let $x(t)$ be defined as the non-stationary frequency hopping analytic signal:

$$x_a(t) = e^{i2\pi f_1 t} [u(t) - u(t - T_{hop})] + e^{i2\pi f_2 t} [u(t - T_{hop} + 1) - u(t - T)], \quad 0 \leq t \leq T, \quad (2.2)$$

where T_{hop} is the hopping time at which point the message frequency hops from frequency f_1 to f_2 , and $u(t)$ is the unit step function defined as :

$$u(t) = \begin{cases} 1, & \text{for } t \geq 0 \\ 0, & \text{for } t < 0 \end{cases}. \quad (2.3)$$

Substituting Equation (2.2) into Equation (2.1) leads to [3, pp. 49]:

$$\begin{aligned}
TCF(t, \tau) = & \left\{ \begin{aligned} & e^{i2\pi f_1 \tau} \left[\begin{aligned} & u\left(t + \frac{\tau}{2}\right) \left[u\left(t - \frac{\tau}{2}\right) - u\left(t - \frac{\tau}{2} - T_{hop}\right) \right] \\ & + u\left(t + \frac{\tau}{2} - T_{hop}\right) \left[u\left(t - \frac{\tau}{2} - T_{hop}\right) - u\left(t - \frac{\tau}{2}\right) \right] \end{aligned} \right] \\ & + e^{i2\pi f_2 \tau} \left[\begin{aligned} & u\left(t + \frac{\tau}{2} - T_{hop} + 1\right) \left[u\left(t - \frac{\tau}{2} - T_{hop} + 1\right) - u\left(t - \frac{\tau}{2} - T\right) \right] \\ & + u\left(t + \frac{\tau}{2} - T\right) \left[u\left(t - \frac{\tau}{2} - T\right) - u\left(t - \frac{\tau}{2} - T_{hop} + 1\right) \right] \end{aligned} \right] \\ & e^{i2\pi \left[(f_2 - f_1)t + \left(\frac{f_1 + f_2}{2}\right)\tau \right]} \left[\begin{aligned} & u\left(t + \frac{\tau}{2} - T_{hop} + 1\right) \left[u\left(t - \frac{\tau}{2}\right) - u\left(t - \frac{\tau}{2} - T_{hop}\right) \right] \\ & + u\left(t + \frac{\tau}{2} - T\right) \left[u\left(t - \frac{\tau}{2} - T_{hop}\right) - u\left(t - \frac{\tau}{2}\right) \right] \end{aligned} \right] \end{aligned} \right\} .(2.4) \\
= & TCF_1(t, \tau) + TCF_2(t, \tau) + TCF_{12}(t, \tau).
\end{aligned}$$

The terms $TCF_1(t, \tau)$, $TCF_2(t, \tau)$, $TCF_{12}(t, \tau)$ respectively correspond to the 1st, 2nd, and 3rd terms included in Equation (2.4). The three terms exist in non-overlapping triangular shaped regions which make up the complete TCF expression. The unit step expressions are used to model the three triangular shaped regions present in the TCF Phase expression shown in Equation (2.4). They are used to depict the boundary lines between the triangular shaped $TCF_1(t, \tau)$, $TCF_2(t, \tau)$, and $TCF_{12}(t, \tau)$ phase regions and have $\pm 45^\circ$ orientations.

Note that the phase of the $TCF_1(t, \tau)$ and $TCF_2(t, \tau)$ terms expressed as a function of the variable “t” are constant and equal to $2\pi f_1 \tau$ and $2\pi f_2 \tau$, respectively, while the phase contribution contained in the term $TCF_{12}(t, \tau)$ varies in terms of both variables t and τ . Therefore, the TCF phase expressed as a function of “t” for a fixed “ τ ” exhibits changes in its slope value when going from one region to another one. Figure 2 illustrates the behavior of the phase of the TCF matrix computed from the signal $x_a(t)$ in Equation (2.2) where

$f_1 = 15\text{Hz}$, $f_2 = 45\text{Hz}$, the hopping time $T_{hop} = 150$, and the total signal duration $T = 300$. Figure 2 shows that the hopping time can easily be extracted at the left most tip of the $TCF_{12}(t, \tau)$ region.

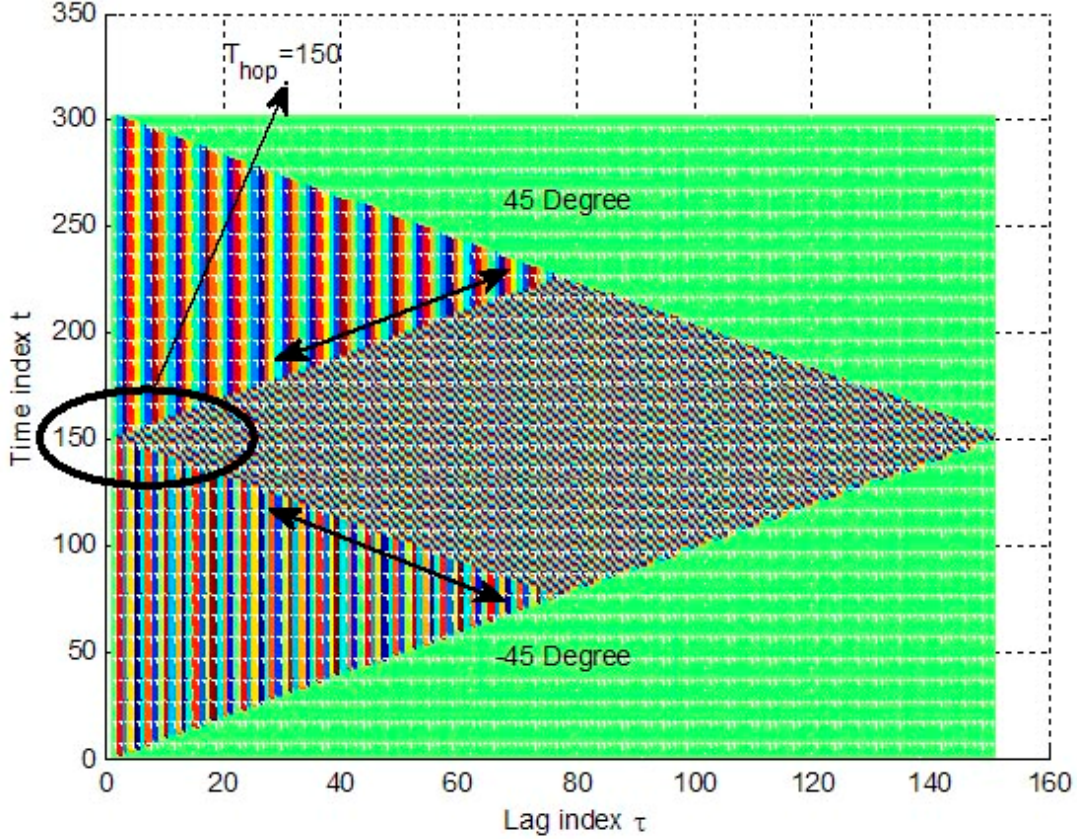


Figure 2. TCF Angle of a Non-stationary Analytic Frequency Hopping Signal; Hopping Time Location at $t=150$.

Changes in the TCF phase behavior as a function of “t” are emphasized with further processing by applying the one-dimensional wavelet transform to emphasize the edges and followed by morphological processing operations to automate the detection of such edges. The Wavelet transform and morphological tools used in this work are discussed later in Sections IV and V.

The overall algorithm designed to detect hopping time locations can be split into three main phases, as illustrated in Figure 3.

- Phase 1: a) Compute the TCF phase matrix $TCF(t, \tau)$ over a short finite time window; b) Differentiate the TCF phase matrix along the time index (keeping τ fixed).
- Phase 2: Compute the one-dimensional wavelet transform of the resulting differentiated TCF phase matrix along the time index (keeping τ fixed).
- Phase 3: Apply image morphological tools to clean the image and extract hopping time information.

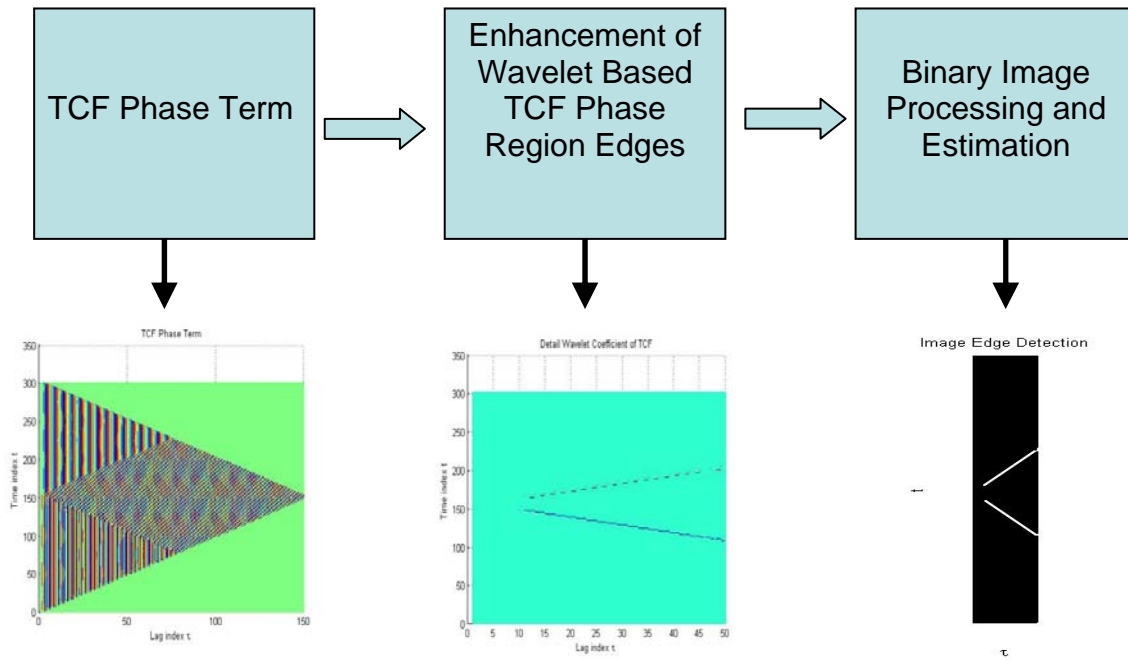


Figure 3. Overall FH Signal Hopping Time Estimation Process; Flow Chart and Intermediary Representative Results for Each Stage.

III. DETECTING IMPROVEMENT TECHNIQUES

We showed in Chapter II that the TCF phase matrix clearly exhibits hopping time locations when little or no noise is present. The actual detection process relies on changes observed between the three TCF phase regions discussed earlier. However, hopping time location information degrades significantly with increasing noise levels. For example, the top plot of Figure 5 shows the TCF phase of the FH signal distorted by additive white Gaussian Noise(AWGN) with SNR=9 dB for lag $\tau = 25$. This example shows that the hopping time information is very hard to extract, as the noise causes random spikes in the phase information. Thus, additional processing becomes necessary to increase the robustness of the detection scheme. This section discusses three such processing steps; unwrapping the phase information, differentiating the phase information to emphasize phase change behavior, and applying a median filter to de-emphasize noise effects.

A. PHASE UNWRAPPING FUNCTION

The TCF phase, $p(t)$, of the signal, $x(t)$, may be unwrapped as [3, pp. 52]:

$$\text{unwrap}(p(t)) = \begin{cases} p(t) & , \text{if } |p(t) - p(t-1)| \leq \pi \\ p(t) + 2\pi & , \text{if } p(t) - p(t-1) < -\pi \\ p(t) - 2\pi & , \text{if } p(t) - p(t-1) > \pi \end{cases} \quad (3.1)$$

Note that phase unwrapping transforms jumps larger than π between successive points to their 2π complement. Figure 4 shows the results obtained by unwrapping the TCF phase function along the time axis (while the parameter τ is kept constant). Note that the phase exhibits constant values for times between $[0 \ 100]$ and $[160 \ 256]$. These sections correspond to the TCF_1 and TCF_2 regions where the phase is constant (when expressed as a function of t , for a fixed value of τ). The phase behavior in the TCF_{12} region is expected to be linear (when expressed as a function of t for a fixed τ value), as was shown

earlier in Equation (3.1). However, noise distortions result in multiple phase jumps in the TCF_{12} region, i.e., for times in the range [100 160]. These multiple jumps can be cleaned up by unwrapping the phase, as shown in the bottom plot of Figure 5. Note that the slope of the TCF_{12} region is linear, as expected, after applying the unwrapping function, and the plot now exhibits a large gap value between TCF_1 and TCF_2 regions.

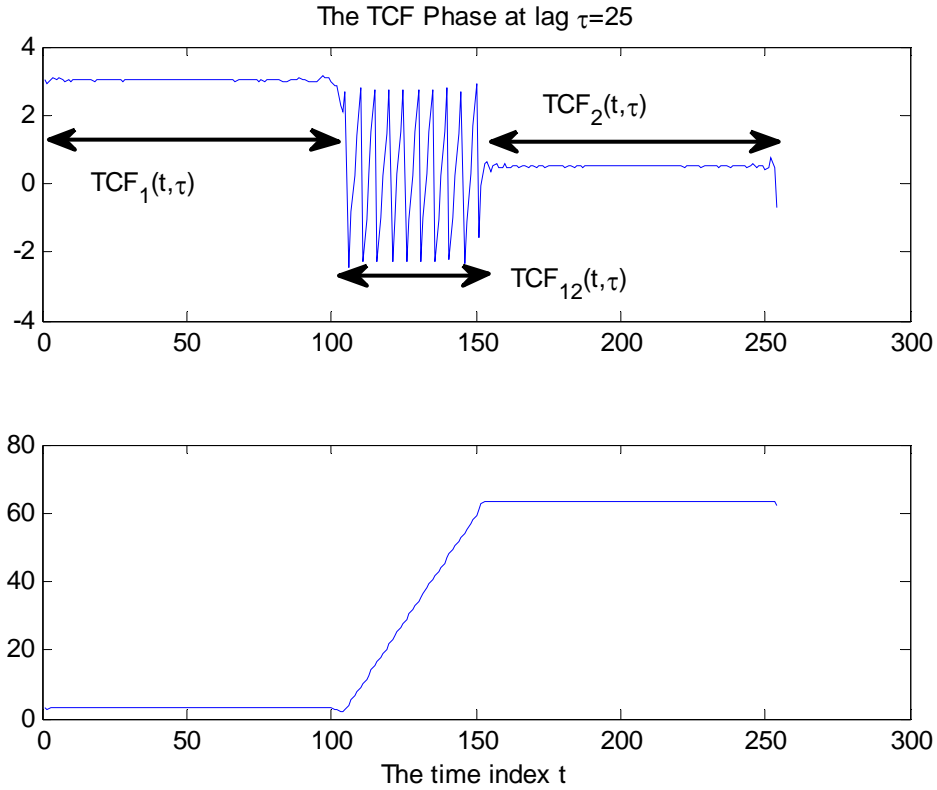


Figure 4. Unwrapping Function Impact on the TCF Phase Function; Hopping Time Location at $t=125$; Noise-Free Signal Case.

Unwrapping the phase function along the time axis (while the variable τ is kept constant) is useful as the noise level increases when sudden phase jumps may occur in TCF_1 or TCF_2 regions with theoretical constant phases (when considered as a function of t , with τ fixed), as illustrated in Figure 5. Note the random phase jumps in the intervals [0 100] and [160 256] which corresponds to

the TCF_1 and TCF_2 regions where the phase is expected to be constant in noise-free cases. After the unwrapping step, the phase behavior in TCF_1 and TCF_2 regions exhibit very small variations due to the noise, and the TCF_{12} region phase is again linear.

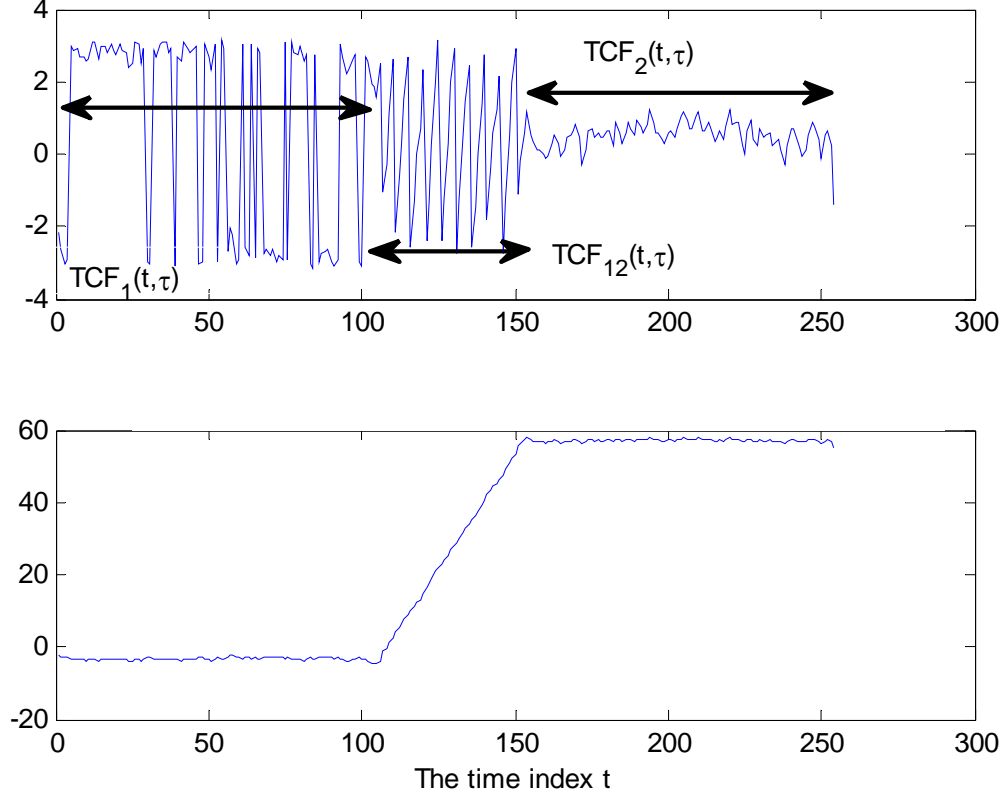


Figure 5. Unwrapped TCF Phase Term at Lag $\tau=25$, SNR=9 dB.

B. DIFFERENTIATION

Recall the expected TCF phase behavior expressed as a function of t , while keeping τ fixed is a succession of three lines; flat lines in the TCF_1 and TCF_2 regions, while it is a ramp in the TCF_{12} region. This behavior represents two discontinuities in the phase expressed as a function of t (while keeping τ fixed),

which are emphasized by differentiating the phase along the time axis. Recall the first derivative of a line is equal to its slope and is defined as:

$$slope = \frac{m_2 - m_1}{t_2 - t_1} = \frac{\text{amplitude difference}}{\Delta t}. \quad (3.2)$$

The differentiation function computes the difference between adjacent points. Differentiating the unwrapped TCF phase along the time axis results in a pulse where the ramp used to be, and zero otherwise. Such a step further emphasizes the difference between the auto-term and cross-term regions, as illustrated in the bottom plot of Figure 6.

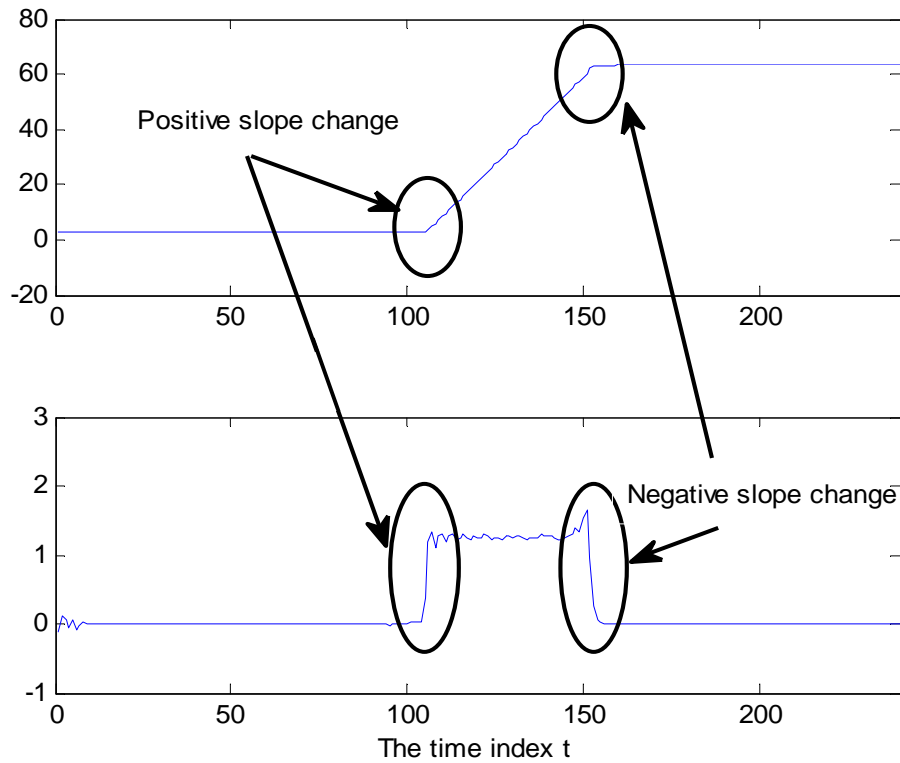


Figure 6. Unwrapped TCF Phase Term; Differentiation Step Applied to the Unwrapped TCF Phase Along the Time Axis, τ Fixed.

C. MEDIAN FILTER

Note that the basic differentiation operation used above also emphasizes high frequency noise. For example, Figure 6 above exhibits small variations within the expected constant regions, or the linear ramp region. Such discontinuities can be smoothed out by using a median filter which is designed to remove short-term spike distortions while maintaining long-term signal trends.

The median filter is a non-linear filter commonly applied to remove isolated outliers or short discontinuities. In this filter, input points are sorted by increasing values, and the middle point picked as the filter output. Thus, isolated outliers are not selected as outputs and short-term distortions can be discarded by selecting a median filter of length high enough. Figure 7 shows the median filter output to the signal shown in the top plot for a median filter of length 30. The figure shows the small oscillations present on the pulse disappeared without affecting the overall shape of the 50-point wide square pulse, as the pulse width is longer than the selected median filter length.

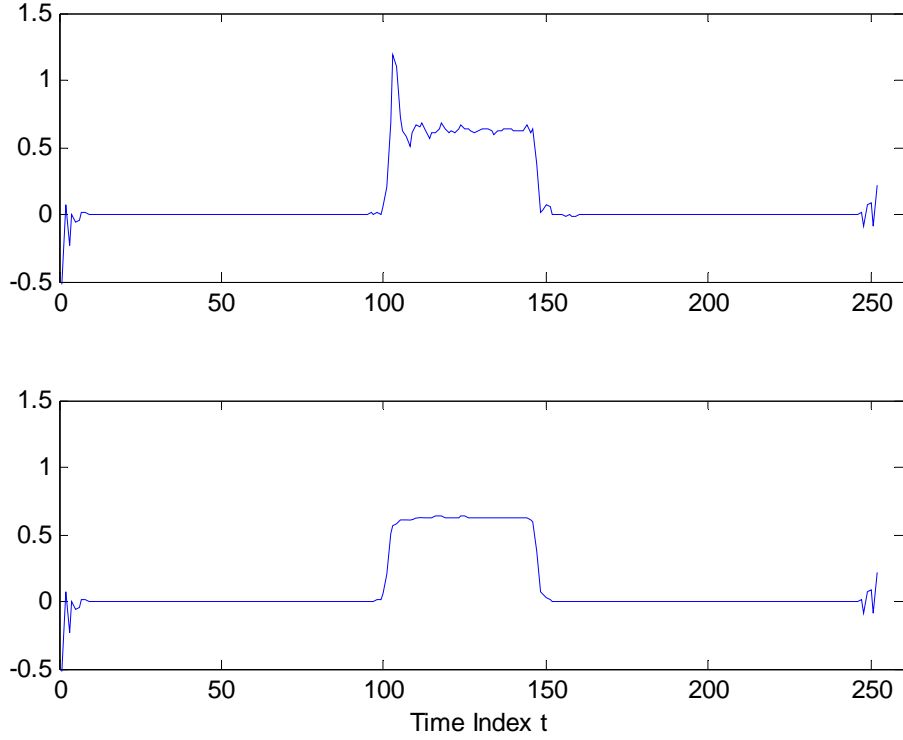


Figure 7. Median Filter Impact on Pulse-Like Signal; Top Plot: Original Signal, Bottom Plot: Median Filter Output with Median Filter of Length 30.

D. NO-HOP SIGNAL CASE: SHORT-TERM VARIANCE TRACKING DECISION SCHEME

All processing schemes previously discussed focus on emphasizing the phase changes between the different TCF phase regions to better detect hopping time locations. However, we need to also consider the case when no hop occurs in the time frame under investigation. In such cases, the TCF phase plot expressed as a function of time (keeping τ fixed) is constant, when there is no noise distortion. However, noise introduces artifacts in the TCF phase which may result in isolated spikes, as illustrated in Figure 8. In such a case, phase unwrapping may still result in artificial discontinuities and subsequent median filtering steps are not sufficient to eliminate short term discontinuities in the TCF phase behavior (expressed as a function of t). Figure 8 (e) illustrates an example

where the TCF phase still exhibits discontinuities after phase unwrapping, differentiation and median filtering.

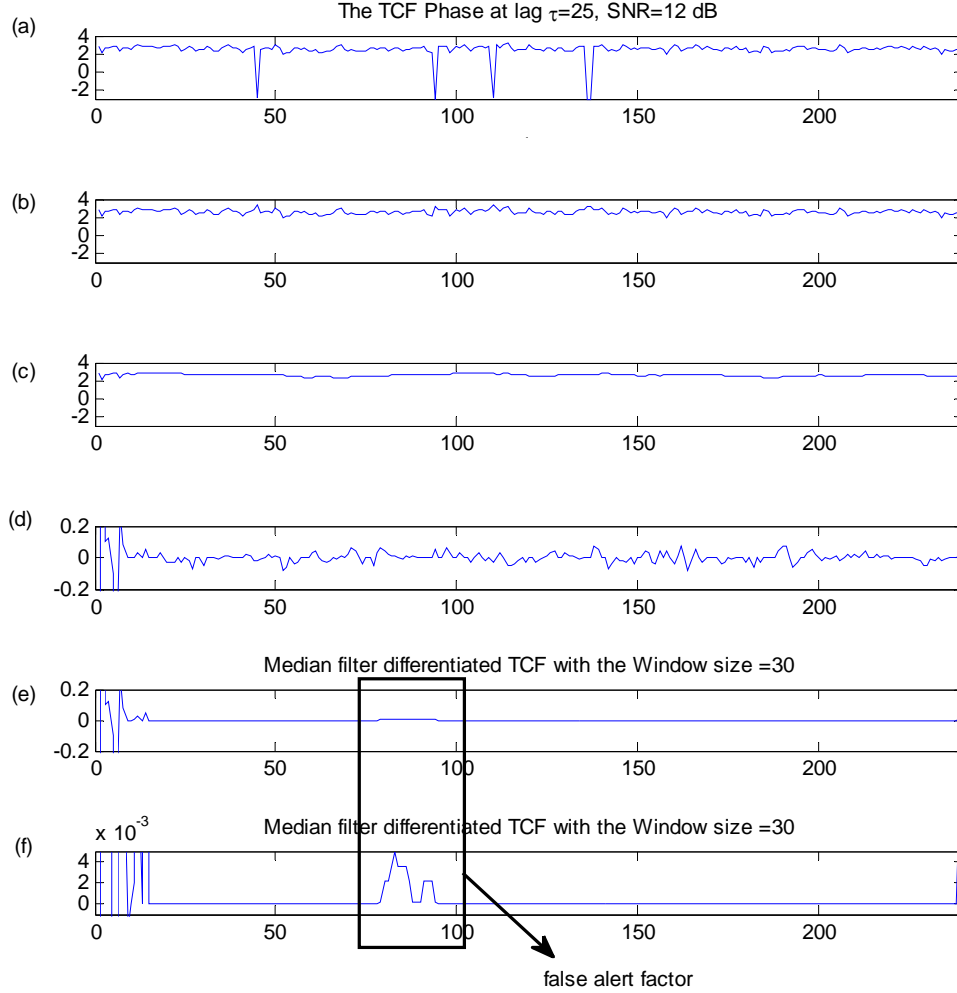


Figure 8. Impact Due to Successive Operations Applied to the TCF Phase for the No-hop Signal Case, $TCF(t, \tau)$ for $\tau = 25$ Fixed, SNR=12dB: First median Length=15, Second Median Length=30; (a) Original TCF Phase, (b) After Phase Unwrapping, (c) After Median Filtering, (d) After Differentiating, (e) & (f) After Second Median Filter.

Figure 8 (e) & (f) show two discontinuities remain after applying the 2nd median filter. Such discontinuities will be emphasized by the wavelet transform

and may later result in an incorrect hop decision. Thus, we investigated a different approach to first evaluate whether a hop is present somewhere in the time frame or not, prior to applying phase unwrapping on the $TCF(t, \tau)$ expression. Recall that the expected TCF phase term expressed as a function of the variable “t” is constant only when there is no hop in the collected frame, and that changes are expected to occur when a hop is present. Further, recall that noise distortions introduce variations in the TCF_1 and TCF_2 regions which have theoretical constant phase regions, while the phase in the TCF_{12} region exhibits repeated jumps due to noise effects. Figure 9 shows plots of the initial TCF phase before unwrapping is applied for a SNR level equal to 9dB for with-hop and no-hop cases. Note that phase variations in the no-hop case are significantly smaller, due to the absence of the repeated jumps in the TCF_{12} region located in the interval [100 150].

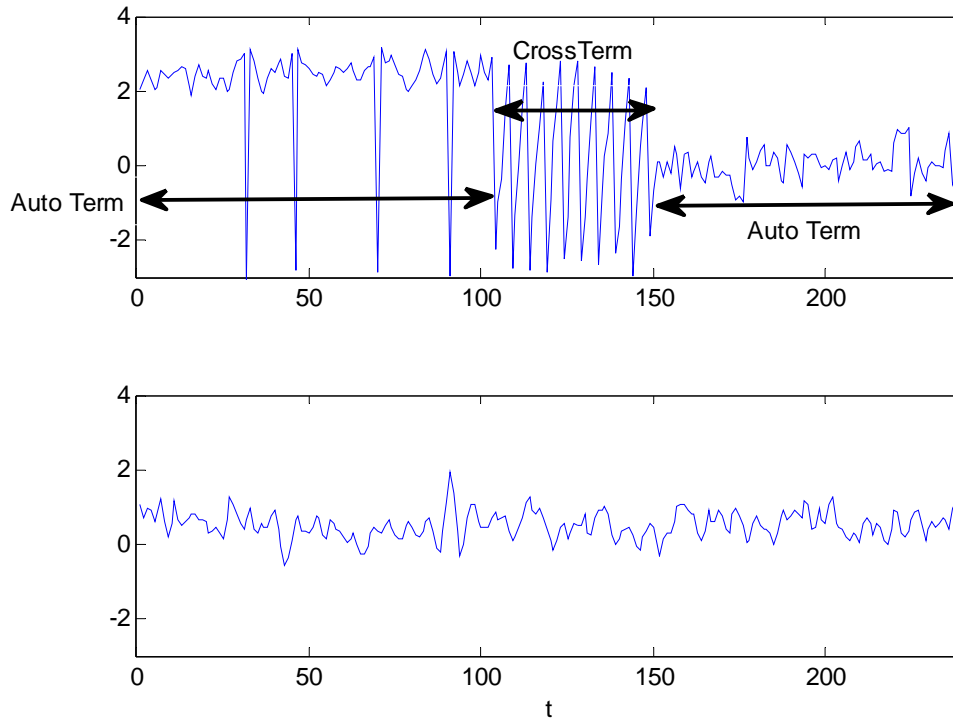


Figure 9. $TCF(t, \tau)$ Phase Plot for Lag $\tau = 25$; SNR=9dB; Top Plot: One-hop Signal Case, and Bottom Plot: No-hop Signal Case.

Thus we implemented a simple ad-hoc scheme which tracks changes in the TCF phase variance for a specific lag value before phase unwrapping is applied. We split the TCF phase function (expressed in terms of t , for a fixed lag τ) into 10 non overlapping windows, and compute the variance of each. Table 1 illustrates the resulting process for the two TCF phase plots shown in Figure 9. In this example, the overall variance for the one-hop and no-hop signal cases are equal to 2.2328 and 0.0032, respectively. Note that estimated variance values exhibit larger variations in the one-hop case than those observed in the no-hop case, due to the repeated phase jumps in the [100 150] interval occurring in the TCF_{12} region for the one-hop signal case.

Sub-window	1	2	3	4	5	6	7	8	9	10
One Hop Signal TCF phase variance	0.05	2.46	1.24	1.33	4.08	3.32	0.13	0.15	0.2	0.1
Variance between each sub-window	2.2328									
No Hop Signal TCF phase Variance	0.07	0.17	0.07	0.26	0.13	0.1	0.14	0.1	0.1	0.12
Variance between each sub-window	3.20E-03									

Table 1. TCF Phase Short-Term Variances Computed within the Estimation Frame; 10 Non-Overlapping Sub-Windows; One-Hop and No-Hop Cases.

Thus, we discriminate between no-hop and with-hop scenarios using the variation in short-term variance values. By trial and error, we selected a threshold value equal to 1 to conduct a first attempt at deciding between no-hop or one-hop cases; signal frames leading to TCF phase short-term variance values below 1 are said to contain no hop within the frame. Note the threshold value selected was quite conservative in the sense that it was set to decide “no-hop” on only the most obvious cases. When a signal frame is detected to have a hop in this first stage, further processing can still lead to a no-hop decision later. Specific details

on the overall decision scheme are presented later in Section VI. Figure 10 presents no-hop decision results obtained with this ad-hoc decision scheme.

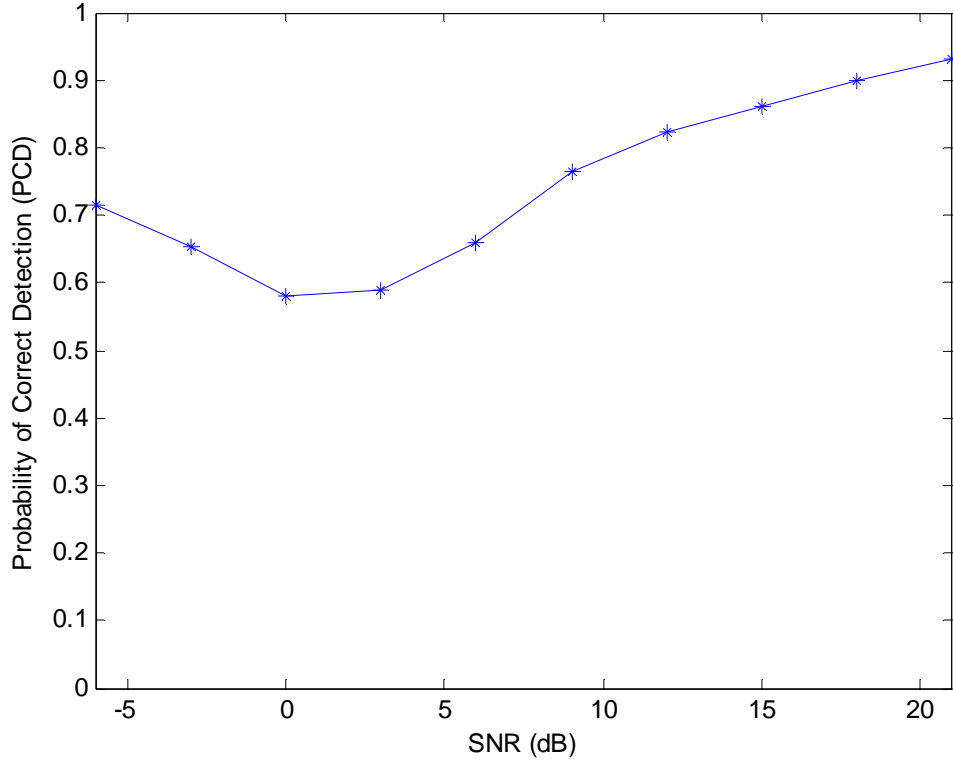


Figure 10. Probability of Correct Detection Using the TCF Phase Short-term Variance Thresholding Scheme; No-hop Scenarios Only, Random Frequency, 250 Experiments, SNR Level Between -6 to 21 dB.

IV. WAVELET TRANSFORM

In Chapter III we showed that the TCF phase term shows step discontinuities between three regions when the sample FH signal contains a hop, as illustrated in Figure 7. This step discontinuity presents a high frequency signal which is used to estimate the hopping time location in this thesis. Various signal processing operations can be used to extract signal or image discontinuities. This thesis uses the Wavelet transform which is briefly introduced in this chapter.

A. INTRODUCTION

The Fourier transform is used to represent a time domain signal in the frequency domain. The transformation is defined as [5]:

$$x(f) = \int_{-\infty}^{\infty} x(t)e^{-2i\pi ft} dt. \quad (4.1)$$

The Fourier transform $x(f)$ is well suited when dealing with stationary signals as it shows the contribution of all frequencies contained in a given time-domain signal. However, it cannot be used to represent signals with time-varying characteristics, as the time information gets lost after this transformation. In cases where preserving the time information is needed, the Short-Time Fourier Transform (STFT) can be used, as it is expressed in terms of both time and frequency indices. The STFT is defined as [5]:

$$STFT(\tau, f) = \int x(t)g^*(t - \tau)e^{-2i\pi ft} dt, \quad (4.2)$$

where the function $g(t)$ is a finite time sliding window centered at τ . The length of the window function $g(t)$ is selected so that the signal is stationary over the window length. The length of the time window also relates to the time and frequency resolutions of the transform, as a direct result of the Uncertainty Principle. One of the major drawbacks of the STFT is the fixed time and frequency resolution once the window length is selected, resulting in time-frequency partitioning as illustrated in Figure 11 (a).

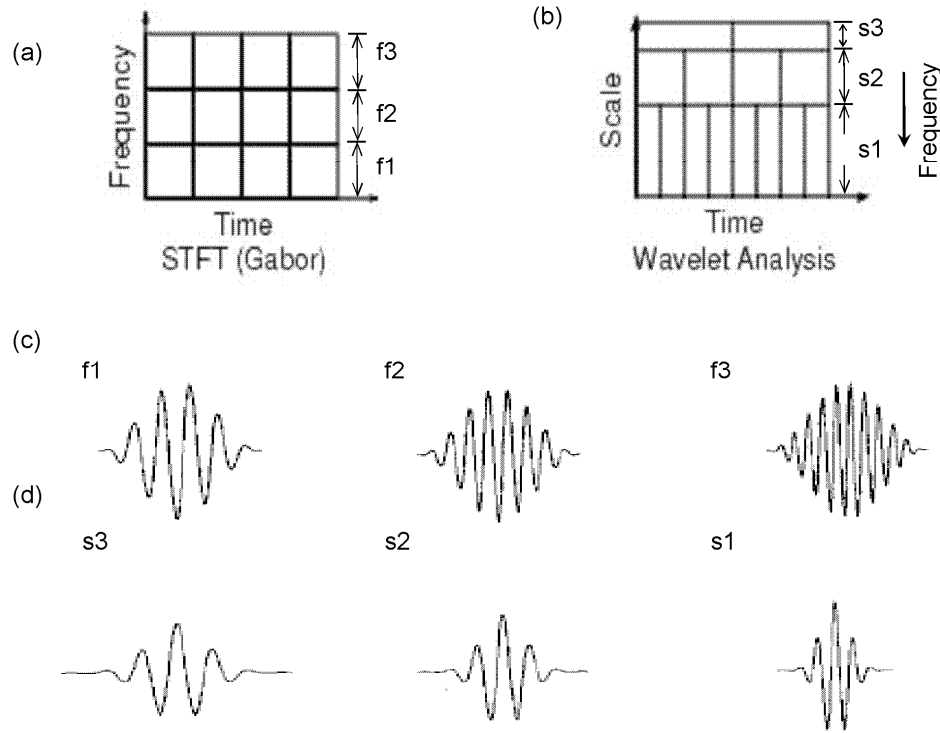


Figure 11. STFT and Wavelet Analysis Time and Frequency Resolution Plot, (a) STFT Frequency vs. Time 2-D plot, (b) Wavelet Analysis Scale vs. Time 2-D plot, (c) STFT Window Examples, (d) CWT Window Examples. [After 6, 7].

As a result, the STFT does not have a variable time-frequency resolution which would be useful for signals with time varying behavior. The Wavelet transform, which can be viewed as an alternative to the STFT, does not have fixed time-frequency resolution. As a result, it is better suited to handle signals with sudden discontinuities, as those present in the TCF phase.

B. CONTINUOUS WAVELET TRANSFORM (CWT)

The continuous Wavelet transform (CWT) of a signal $x(t)$ is defined as:

$$CWT_x(\tau, a) = \frac{1}{\sqrt{|a|}} \int x(t) h\left(\frac{t-\tau}{a}\right) dt, \quad (4.3)$$

where $\frac{1}{\sqrt{|a|}} h(\frac{t-\tau}{a})$ is a scaled and shifted version of the wavelet function $h(t)$.

The scale variable is a , and the time shift variable is τ .

The scale variable a is inversely proportional to the frequency variable, and the scale factor is defined as:

$$Scale = \log_{10}(a). \quad (4.4)$$

Figure 11 (b) and (d) illustrate the time varying nature of the time-frequency resolution provided by the Wavelet transform. Figure 11 (b) shows that the partitioning has good time resolution at high frequencies, and vice versa.

Figure 12 shows Daubechies Wavelet (db) functions for different orders. Highpass and lowpass decomposition filters are shown in blue, and green, respectively. Figure 12 (d) also shows the 15th order Daubechies Wavelet function (referred to as 'db15'). Note that Wavelet functions complexities increase with their order. The 1st order Daubechies wavelet (db1) is used in our work to extract phase discontinuities. This specific wavelet function is also known as the Haar Wavelet.

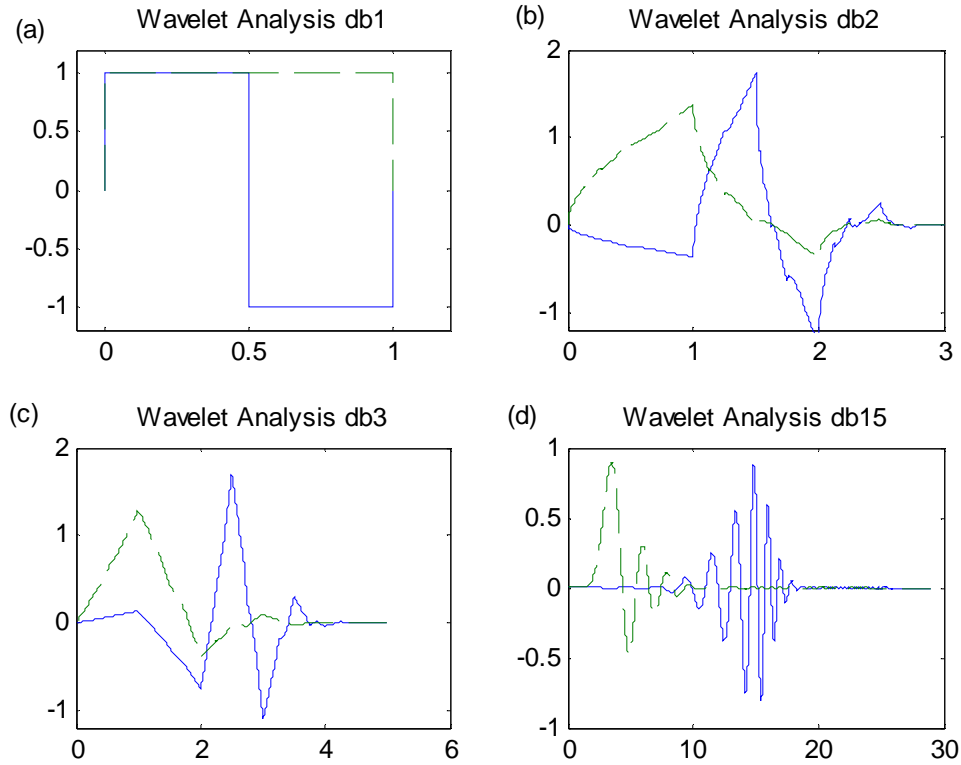


Figure 12. Daubechies Wavelets of Various Orders. Wavelet Highpass Function (blue continuous line), Wavelet Lowpass Function (green dash line).

Figure 13 shows highpass and lowpass Daubechies filters frequency responses for different orders. Note that low order wavelet functions, such as db1 to db3, have long transition regions, while high order wavelet, such as db15, have much steeper and shorter transition regions, becoming closer to ideal filters. However, the filter complexity increases with the filter order.

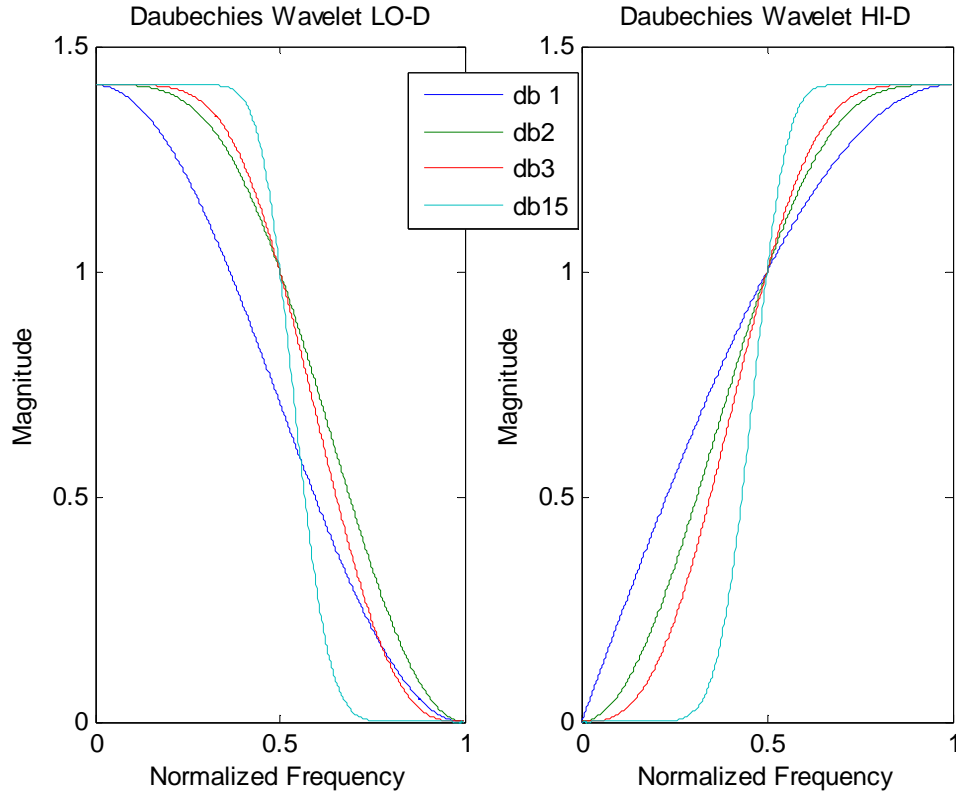


Figure 13. Daubechies Wavelet Analysis Filter Frequency Response, (a) Decomposition LPF Response, (b) Decomposition HPF Response.

C. DISCRETE WAVELET TRANSFORM

As mentioned earlier, the STFT has constant time-frequency resolution partitioning. The STFT can also be viewed as a bank of filters with constant bandwidth, as illustrated in Figure 14 (a). Similar to the CWT, the DWT has a variable time-frequency partitioning, leading to a partitioning of the frequency axis as illustrated Figure 14 (b) for a four-level decomposition. This decomposition can also be represented by the decomposition tree structure shown in Figure 14 (c).

The one-level DWT decomposition operation generates detail and approximation coefficients, which contain the signal high frequency information, and low frequency information, respectively. Note that detail and approximation

coefficients are derived from highpass and lowpass filters and down-sampled by a factor of 2, as the bandwidth has been also decreased by that amount.

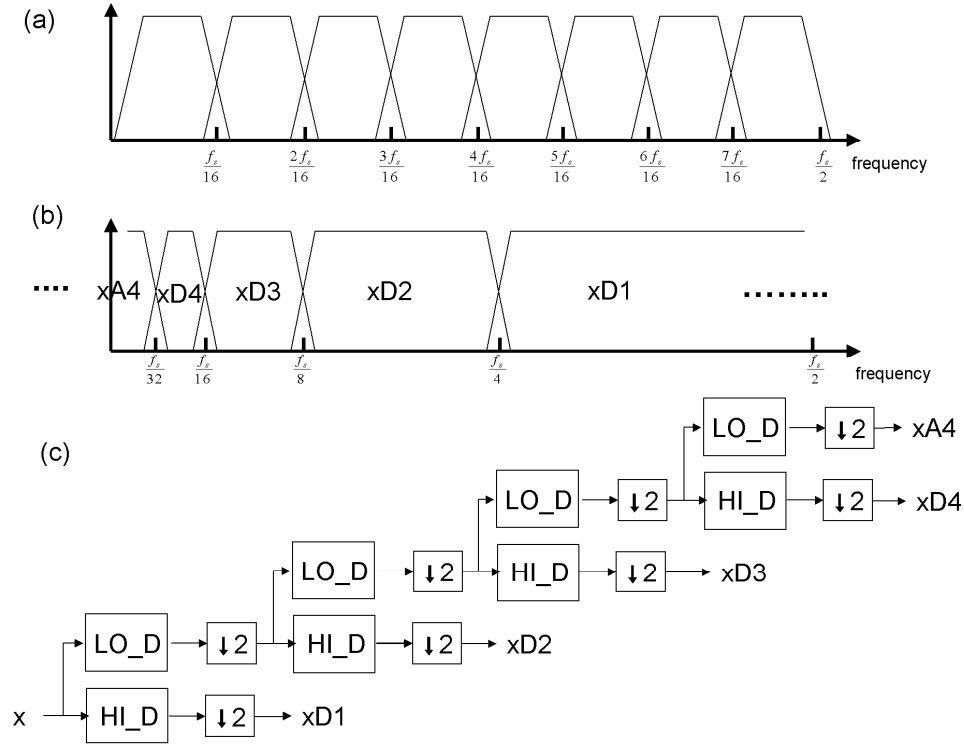


Figure 14. Wavelet Decomposition Filter Bank, (a) STFT Filter Bank, (b) Wavelet Transform Filter Bank, (c) Wavelet Transform Decomposition Tree. [After 5, 8].

Higher level decompositions are obtained by processing the output of successive lowpass filters, where downsampling by 2 is applied at the each filter output. These successive filtering and downsampling operations present in the DWT operation have led to fast DWT implementations. Note the CWT does not include downsampling steps, resulting in a higher complexity transformation.

D. WAVELET ANALYSIS EXAMPLE

We selected the 1st order Daubechies Wavelet (db1) in our work to extract the TCF phase discontinuities. We consider both the DWT and CWT operations and report on their differences.

1. DWT Analysis

Figure 15 (a) shows a representative TCF Phase plot obtained for a fixed lag value $\tau = 25$ from no noise signal. The TCF phase plot exhibits a clear pulse in the trace. Figure 15 (b) shows the resulting 1st-level DWT detail wavelet coefficients obtained for the Haar wavelet (i.e., for scale parameter $a=2$). Note the wavelet coefficients clearly identify the pulse ends, as the spikes indicate the discontinuities. For convenience purposes and maintain the same dimension as that of the original TCF plot, we reversed the downsampling operation present in the MATLAB DWT transformation by up-sampling the results by 2 (i.e., by adding a zero between successive coefficients). Results are illustrated in Figure 15 (c). Approximation coefficients containing the low frequency signal information are shown in Figure 15 (d). Approximation coefficients were not used in our detection scheme.

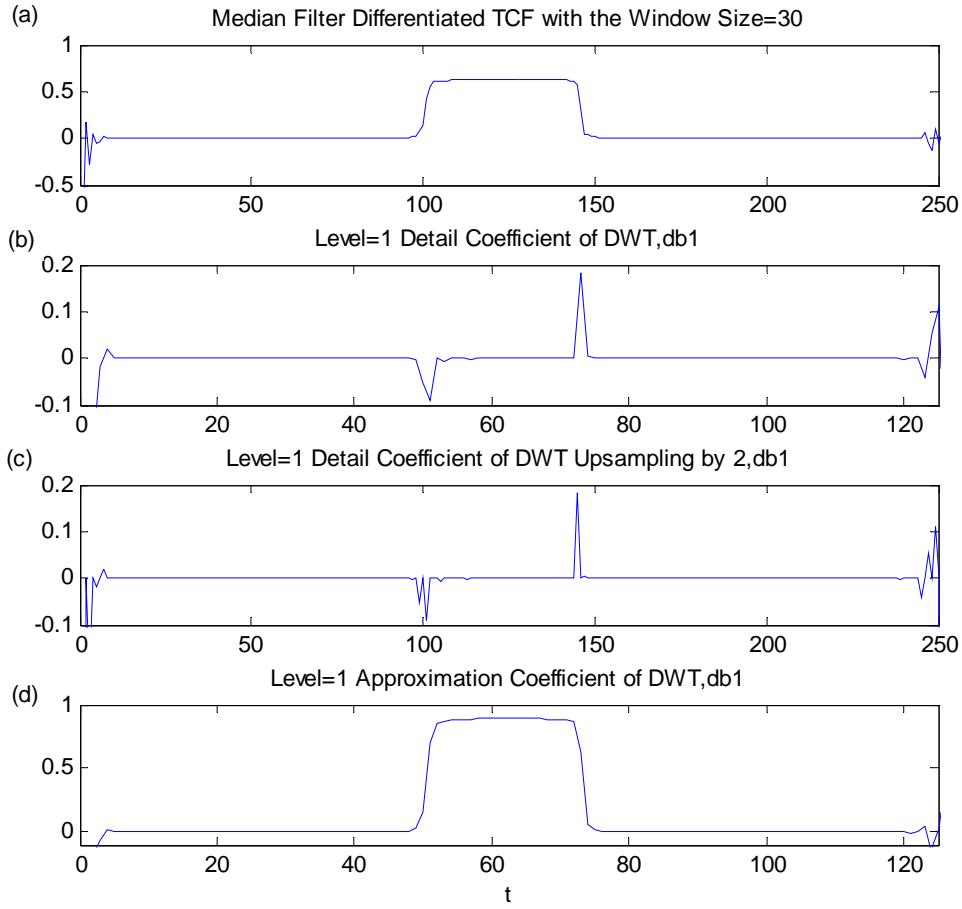


Figure 15. Application of the DWT to the Processed TCF Phase for a Fixed Lag Value τ ; (a) TCF Function for a Fixed Lag Value (b) Detail Coefficients, One-Level DWT Transform of (a), Haar Wavelet, (c) Detail Coefficients after Up-sampling by 2, (d) Approximation Coefficients, One-Level DWT Transform of (a).

2. CWT Analysis

Figure 16 shows the CWT transformation of the TCF phase plot function considered in Figure 15 (a) for scale values equal to 1, 5, 9, 13, and 17. Results show that the first scale value ($a=1$) is not well suited to extracting the pulse discontinuities but that higher scale values can be use to do so. Figure 15 (b) shows that a scale value equal to five identifies the two pulse edges accurately with the two spikes located around 100 and 146. Figure 15 also shows that these

two spikes get larger as the scale value increases, which is to be expected as the time resolution decreases for lower frequencies.

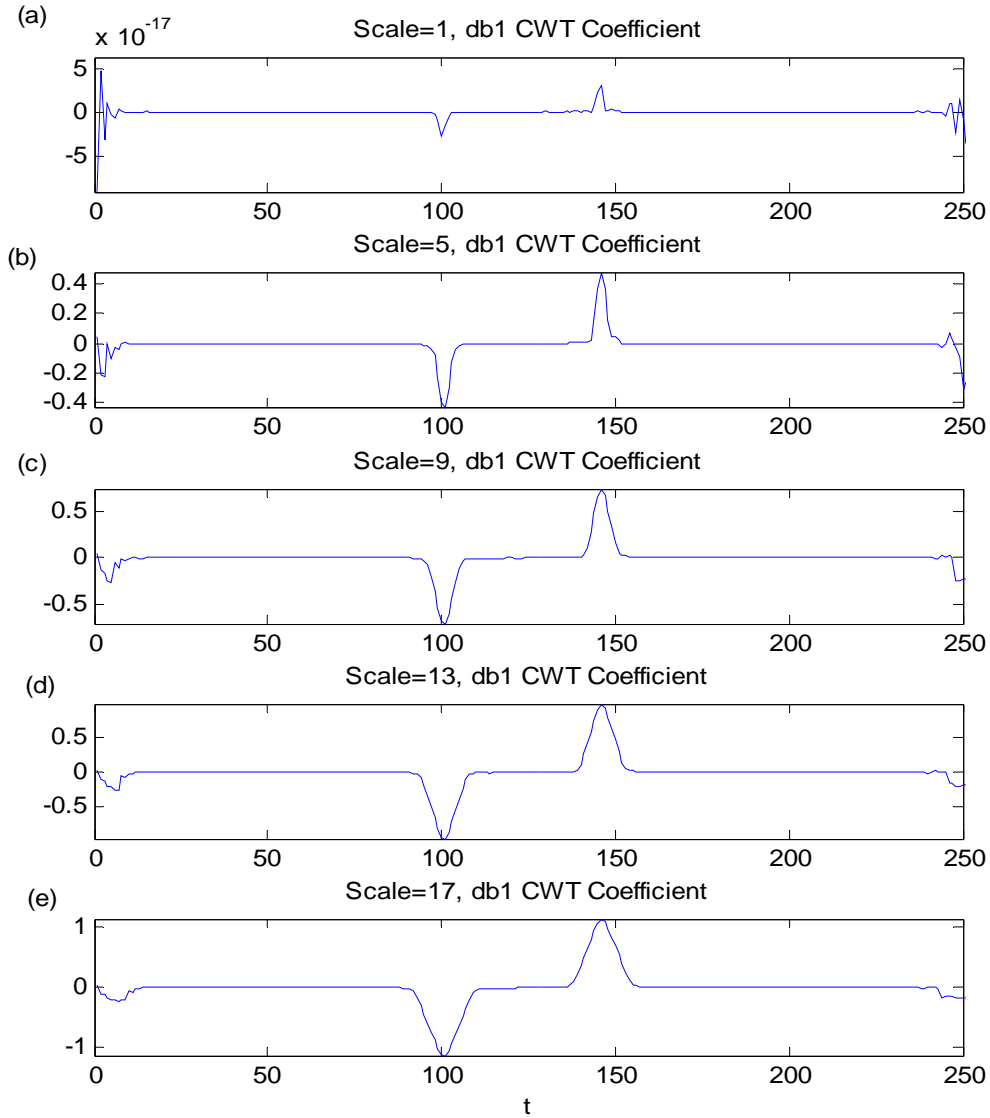


Figure 16. Application of the CWT to the Processed TCF Phase shown in Figure 15(a), (Haar Wavelet); (a) Coefficients for Scale=1, (b) Coefficients for Scale =5, (c) Coefficients for Scale =9, (d) Coefficients for Scale =13, (f) Coefficients for Scale =17.

THIS PAGE INTENTIONALLY LEFT BLANK

V. IMAGE DETECTION AND ANALYSIS

Chapter IV showed that the Wavelet transform can be applied to emphasize the discontinuities present in the TCF phase which are later used to detect the hopping time location. This section introduces the image processing tools used in this thesis to identify the hopping time locations. First, we discuss edge detection schemes. Next, we present, image morphological operation applied to regularize and enhance the TCF image. Finally, we describe how the Hough transform is applied to evaluate the actual hopping time.

A. EDGE DETECTION

Edge detection has been a topic of intense research in image processing over the years, as image edges carry a significant amount of information. Applications are commonly found in an ever wider range of areas, as a result of the improvement in computational power capabilities. Applications can be found in manufacturing with automated categorization of parts, assistive driving schemes for automotive applications, radiology for medical applications, etc... Human activities categorization has also recently received a significant amount of interest due to increased concerns with security applications. In many of these applications, a gray scale or color image is first transformed into a binary image to simplify later stages of the process, which raises issues with level thresholding.

The pattern in an image is represented by the pixels which are split into a finite number of levels after quantization. For example, 8-bit quantization provides $2^8 = 256$ possible intensity levels for each pixel, and the pixels contained in sections with the same colors and intensity will have closer values than those associated with discontinuous portions. A significant amount of the image information is contained in the gradient values, and a significant portion of the image information may be represented by preserving the pixels with large gradients only. Thus, basic edge detection algorithms are based on information

derived from the gradient of the image pixels values [9], as the gradient exploits sudden changes in pixel values found at the region boundaries.

1. First Order Gradient

The simplest method designed to approximate the first order gradient along a particular axis computes the intensity level difference between two adjacent pixels along that axis. Equation(5.1) [9] derives the expression for the pixels energy gradient approximation $g_x(x, y)$ along the x-axis from the original values $p(x, y)$. Similarly, Equation (5.2) shows the expression $g_y(x, y)$ for the first order gradient approximation along the y-axis.

$$g_x(x, y) = \left. \frac{\partial p}{\partial x} \right|_{(x,y)} = p(x, y) - p(x-1, y), \quad (5.1)$$

$$g_y(x, y) = \left. \frac{\partial p}{\partial y} \right|_{(x,y)} = p(x, y) - p(x, y-1). \quad (5.2)$$

2. Sobel Operator

The previous first order gradient approximation is simple but sensitive to noise distortions. In image processing, the first order spatial gradient approximation often uses a Sobel operator that introduces smoothing in the gradient computation by weighting the pixels used in the gradient estimation [9]. Equations (5.3) and (5.4) show the first order gradient approximation applied by the Sobel operator along the x-axis.

$$g_x(x, y) = \left. \frac{\partial p}{\partial x} \right|_{(x,y)}, \quad (5.3)$$

$$\Rightarrow g_x(x, y) = p(x+1, y-1) + 2p(x+1, y) + p(x+1, y+1) \cdots - p(x-1, y-1) - 2p(x-1, y) - p(x-1, y+1). \quad (5.4)$$

Similarly, Equations (5.5) and (5.6) show the first order gradient approximation by the Sobel operator along the y-axis:

$$g_y(x, y) = \left. \frac{\partial p}{\partial y} \right|_{(x,y)}, \quad (5.5)$$

$$\Rightarrow g_y(x, y) = p(x-1, y+1) + 2p(x, y+1) + p(x+1, y+1) + \dots - p(x-1, y-1) - 2p(x, y-1) - p(x+1, y-1). \quad (5.6)$$

Figure 17 shows the edges detected by the Sobel operator on a gray scale image. First, the original gray scale image (top figure) is transformed to black-and-white binary format. Next, the Sobel operator with window size 3 is applied, resulting in the figure shown at the bottom of Figure 17. Note that final edge values usually include some thresholding on gradient values to clean up the results.



Figure 17. Edge Detection Using the Sobel Method, Operator Window Size Equal to 3.

B. IMAGE MORPHOLOGICAL OPERATIONS

Unfortunately, applying edge detection schemes often result in noisy images. Figure 18 shows that a “raw” image may contain much unusable information from the image background itself or from incomplete shapes due to

problems resulting from gradient level threshold steps. For example, a broken blob may still contain many pixels close to each other and accompany several isolated small groups of noisy pixels. Thus, some type of morphological processing is usually necessary to enhance an image and to make it more robust for later stages. Next, we discuss basic morphological operations.

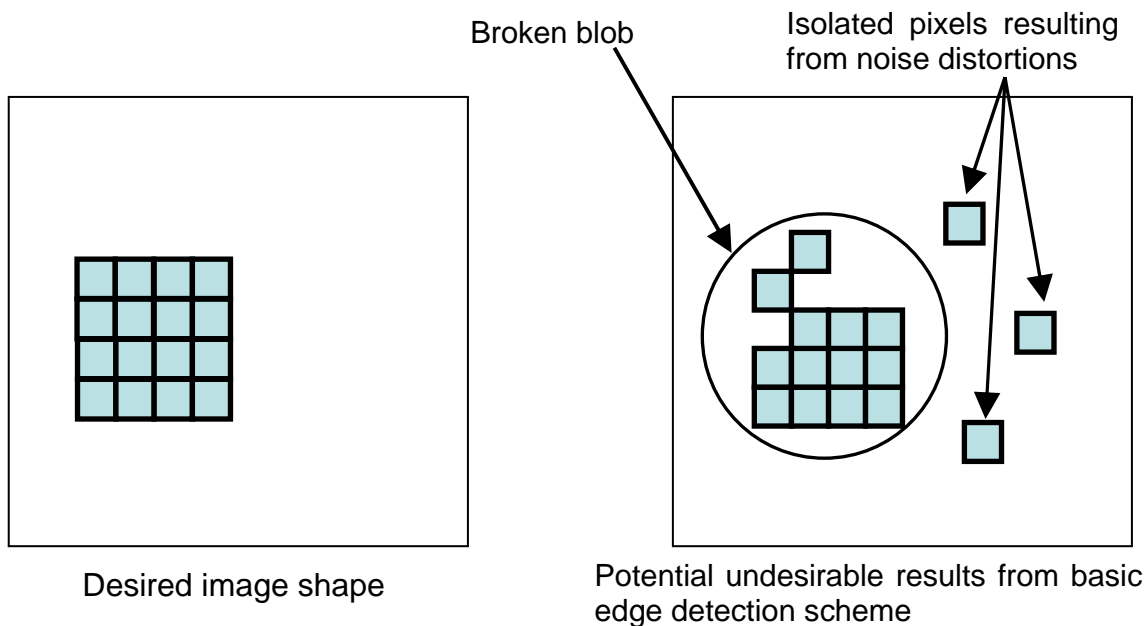


Figure 18. Desired Image Shape and Resulting Potential Image Obtained after Basic Edge Detection Stage [After 10].

1. Dilation

Dilation is the “union” operation between the object and a mask matrix that has a particular alignment fitting a specific figure pixel arrangement. Figure 19 (top plot on the right) illustrates the result obtained after applying a dilation operation. Note that the mask enlarged the original object. The dilation operation fills in small intrusions found in uneven blobs or between broken line segments, resulting in an image with fewer small isolated sections. Note that the dilation operation does not add any redundant information in the image when there is no

original pixel nearby, and the exact type of “fill-in” process depends on the specific mask selected for this operation.

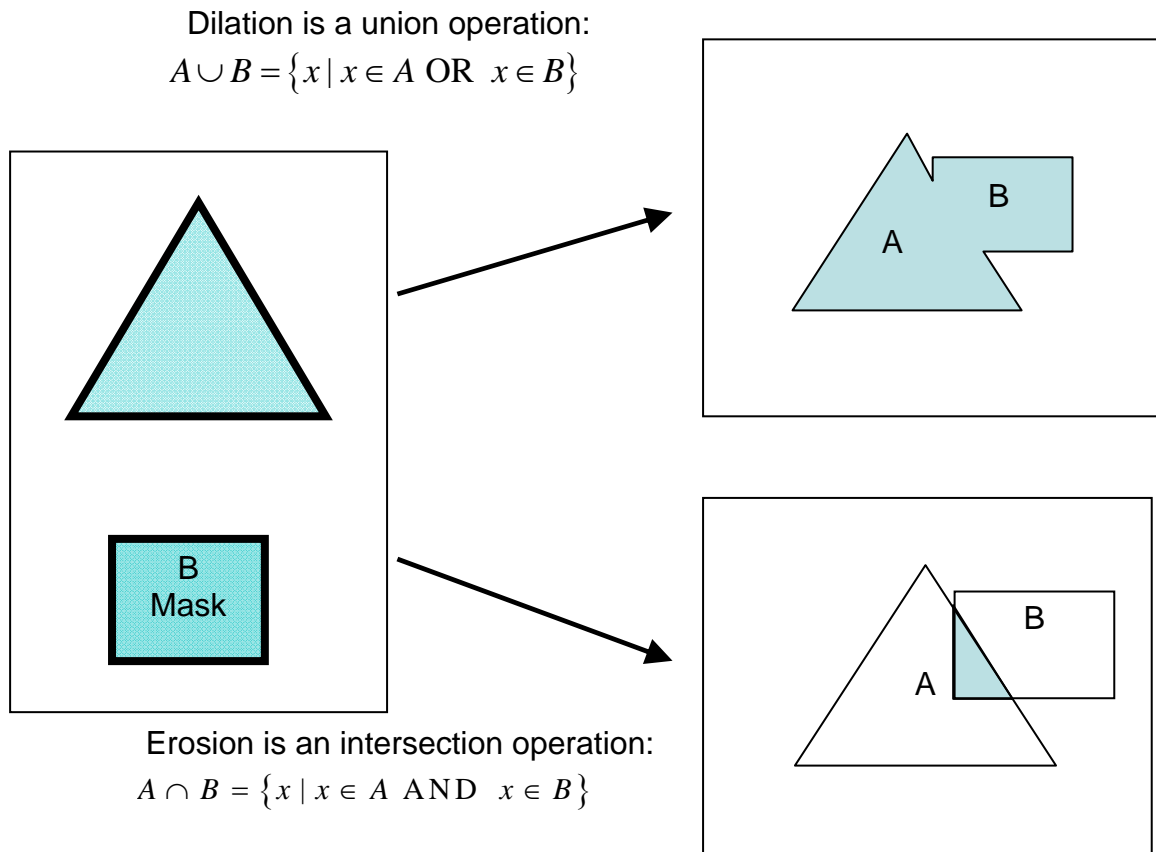


Figure 19. The Logical Operation of Dilation and Erosion [After 10].

2. Erosion

Unlike the dilation operation that extends figure pixel trends when they match the mask selected, the erosion operation removes isolated or small pixel blobs from the image. The erosion operation can be viewed as an intersection operation between the object and mask, as shown in the bottom portion of Figure 19 above. Thus, the erosion mask is designed to remove isolated pixels, as pixels grouping which do not totally enclose the mask matrix are removed.

3. Morphological Operation Example

The mask alignment is crucial to the morphological operation result. The dilation operation interpolates pixels when the mask points reach the original points. Figure 20 illustrates dilation and erosion operation results on a synthetic image block. A few comments can be made:

- The dilation operator extends the isolated pixels and fills in small intrusions found in the broken blob section, resulting in the top plot included in Figure 20.
- The erosion operator removes isolated pixels and significantly shrinks the blob section by removing sections that are smaller than the erosion mask selected for this task.

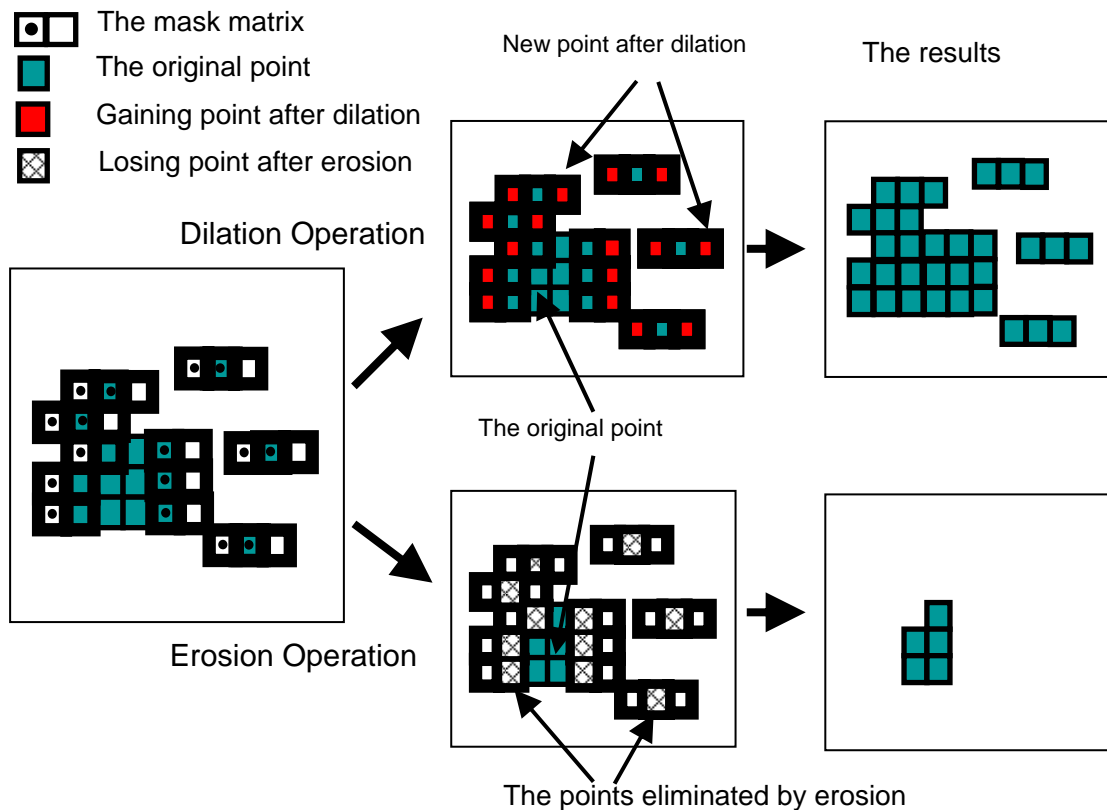


Figure 20. Morphological Operation; 2-bit Landscape Alignment Mask [After 10].

Figure 21 illustrates the dilation masks impacts on the image previously shown in Figure 17. Note the initial image shown at the top of Figure 21 contains numerous isolated segments which outline the road boundaries. The bottom plot in Figure 21 shows the results after applying the dilation operator when the selected mask is a disk with 3-bit radius. Results show the road line sections have become more continuous in nature.

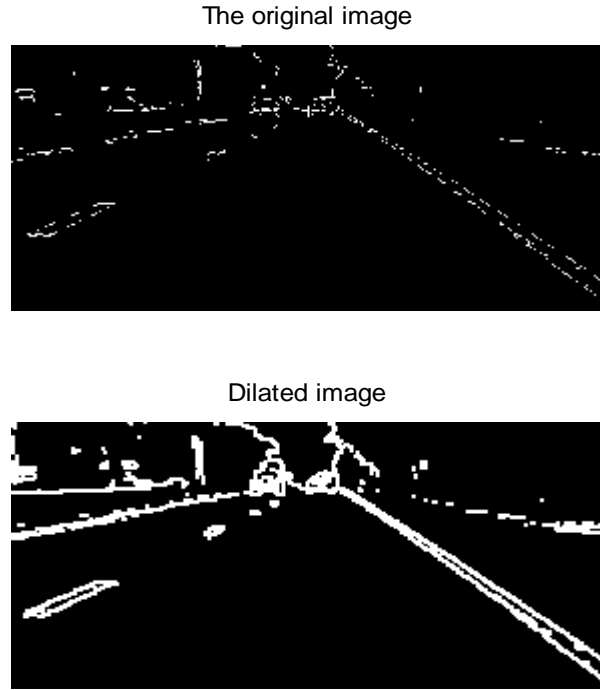


Figure 21. Dilation Operation Impact; 3-bit Radius Mask.

Applying a particular alignment mask, which matches the desired image arrangement, can remove most of the undesirable image pixel contributions. For example, a desired image feature is the road line shown on the right side of the image with has about a -45° orientation. Using a 3-bit window, a potential mask for the erosion operation, the mask matrix may be defined as:

$$\begin{bmatrix} 1 & 0 & 0 \\ 0 & 1 & 0 \\ 0 & 0 & 1 \end{bmatrix}.$$

Applying this mask results in the deletion of isolated pixels which do not align along -45° . The bottom plot of Figure 22 shows the image obtained after the erosion operation followed by a dilation step with the same alignment mask as that present for the erosion operation. Note that the diagonal aligned mask discards most features which do not exhibit a -45° orientation, resulting in the removal of most of the left side of the image.

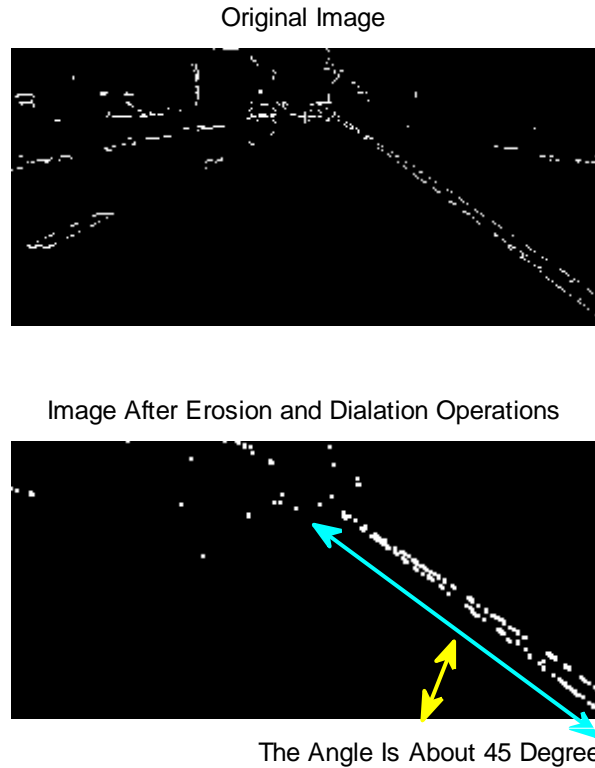


Figure 22. Erosion Mask Orientation Impact, before and after Mask Application; 3-bit Erosion Mask with -45° Orientation.

Figure 23 shows the application of the erosion operator on the wavelet-transformed TCF phase matrix. Two 3-bit erosion masks with 45° and -45° orientations were separately applied to the matrix. The final image results by summing both eroded images. Note the erosion operation removed all separated small pixel groupings except for the groupings aligned along $\pm 45^\circ$.

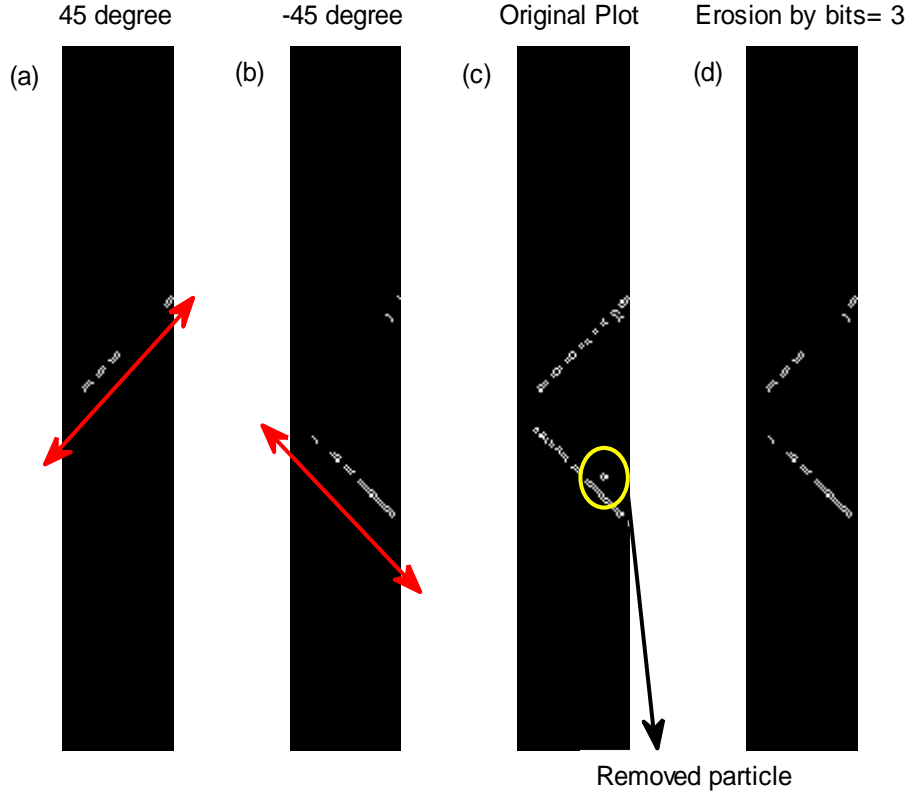


Figure 23. Erosion Operation of the Edge Detected TCF Phase Term with 3-bit Erosion Mask. (a) After 45° Mask Erosion; (b) After -45° Mask Erosion; (c) Original Plot; (d) Final Plot: Summation of (a) and (b).

C. HOUGH TRANSFORM

The Hough transform is commonly used in image processing applications to detect the location and orientation of lines, circles, or ellipses contained within a given image. The Hough transform is used in this thesis to locate the location of the TCF phase region boundaries which lead to hopping time locations.

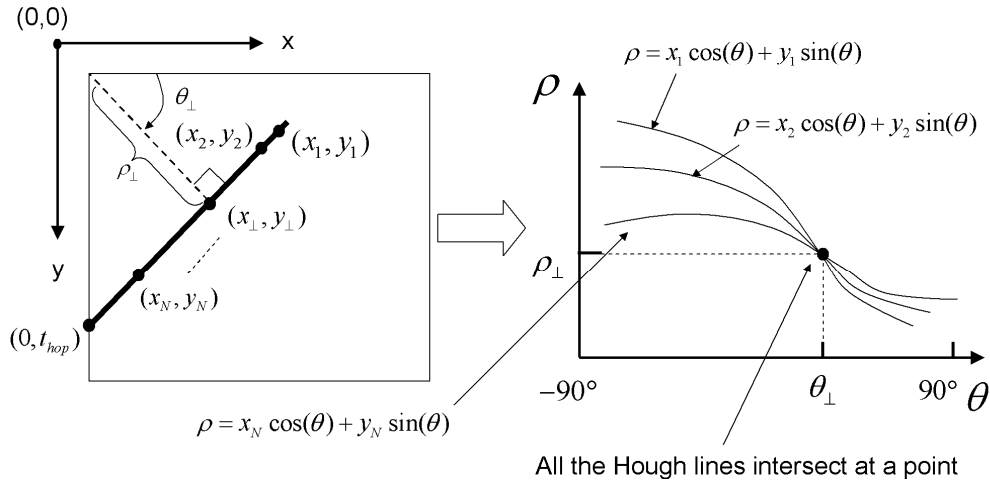
The Hough transform parameterizes a line by representing it in terms of 2 other parameters: θ_\perp and ρ_\perp , which characterize a second line orthogonal to the line of interest (shown in Figure 24 as the dotted line), and passing through the origin (0,0) of the image. The parameter ρ_\perp is the length between the origin of the image and the intersection point with the line of interest, while θ_\perp is the angle

between the x-axis and that second line shown in Figure 24 as the dotted line. Thus, the points with coordinates (x_i, y_i) located on a line parameterized by the angle θ and length ρ may be written as:

$$y_i = -\frac{\cos(\theta)}{\sin(\theta)} x_i + \frac{\rho}{\sin(\theta)}, \quad (5.7)$$

which can be rewritten as:

$$\rho = x_i \cos \theta + y_i \sin \theta. \quad (5.8)$$



Hough lines have to satisfy the equation: $\rho = x_i \cos(\theta) + y_i \sin(\theta)$

Figure 24. Hough Transform and Hough Line Equation [After 11].

Equation (5.8) corresponds to a sinusoidal curve in the (ρ, θ) plane. Figure 24 show that all points on the line will correspond to sinusoidal curves which intersect only at a specific value of ρ and θ shown on the figure as: $(\rho_{\perp}, \theta_{\perp})$ in the Hough transformed plot. Thus finding lines in the original image plane results in finding isolated points in the Hough transformed plane. Once the

parameters $(\rho_{\perp}, \theta_{\perp})$ are identified, the line parameters may be recovered as follows. The coordinates of the point (x_{\perp}, y_{\perp}) on the line which is at the shortest distance θ from the origin are

$$\begin{cases} x_{\perp} = \rho_{\perp} \cos \theta_{\perp} \\ y_{\perp} = \rho_{\perp} \sin \theta_{\perp} \end{cases} \quad (5.9)$$

Those coordinates are used to compute the line slope which is given by:

$$\text{line slope} = \frac{y - y_{\perp}}{x - x_{\perp}}. \quad (5.10)$$

Note the line slope value can also be expressed in terms of the angle θ_{\perp} as $\tan(90^{\circ} - \theta_{\perp})$.

Thus, we get:

$$\tan(90^{\circ} - \theta_{\perp}) = \frac{y - \rho_{\perp} \sin \theta_{\perp}}{x - \rho_{\perp} \cos \theta_{\perp}}. \quad (5.11)$$

Further, note the hopping time information t_{hop} is obtained at the intersection of the line with the y-axis in the TCF phase plot, as illustrated in Figure 23. Thus, the intersection point t_{hop} can be identified by setting $x=0$ in Equation (5.11) which leads to:

$$t_{hop} = y = \rho_{\perp} (\sin \theta_{\perp} - \tan(90^{\circ} - \theta_{\perp}) \cos \theta_{\perp}). \quad (5.12)$$

THIS PAGE INTENTIONALLY LEFT BLANK

VI. DETECTION ALGORITHM AND SIMULATIONS

The hopping time detection scheme can be split in three main phases, which are illustrated in Figure 25; (1) TCF phase computation, (2) Enhancement of the TCF phase region edges using the Wavelet transform, and (3) Identification of the hopped frequency timing information via binary image processing operations. This section presents these three phases and the resulting detection performance results.

A. DETECTION ALGORITHM

Figure 25 presents a general flow chart for the detection scheme.

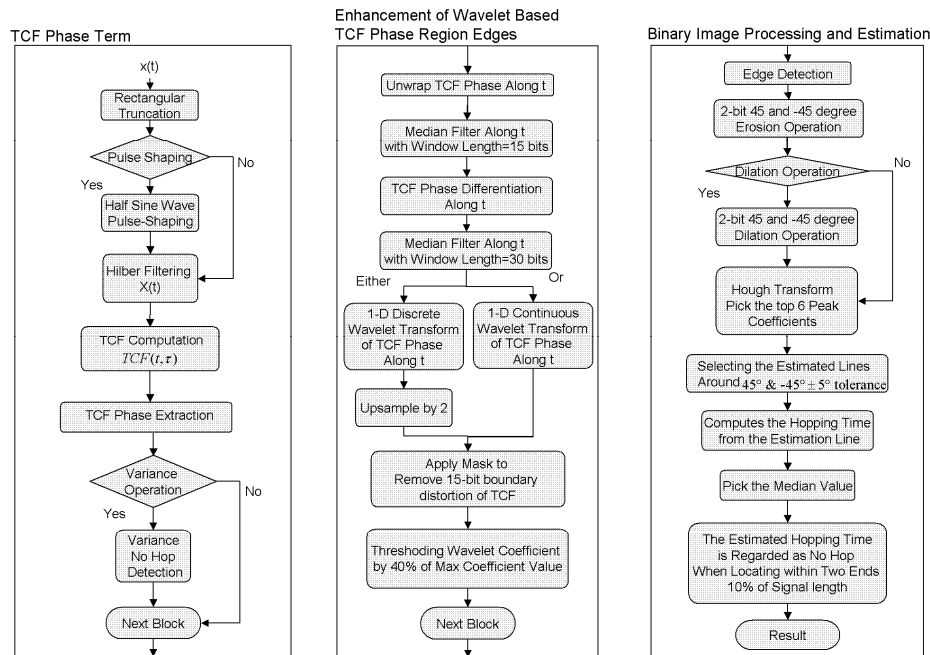


Figure 25. Overall FH Signal Timing Information Detection Algorithm Flow Chart.

1. TCF Phase Term Generation

First, we describe the processing steps conducted in Phase 1 of the detection scheme.

a. FH Signal Generation

Recall this study considers the case where only one frequency hopped signal scheme may be present in a given signal frame. In such a case, the following three scenarios are possible for the received noisy signal frame: 1) one frequency hop, as illustrated in Figure 26, 2) no frequency hop, as illustrated in Figure 27, or 3) multiple hops present within the analysis frame. The multiple-hop case can be avoided by selecting a window frame smaller than that of the shortest signal duration. In addition, the multiple hop case can be treated similarly to that of the one-hop signal case, as it results in a TCF phase with similar basic structures repeating for each hopping event. Thus, for simplicity purposes we assume that we have either one or no hop in the received frame only.

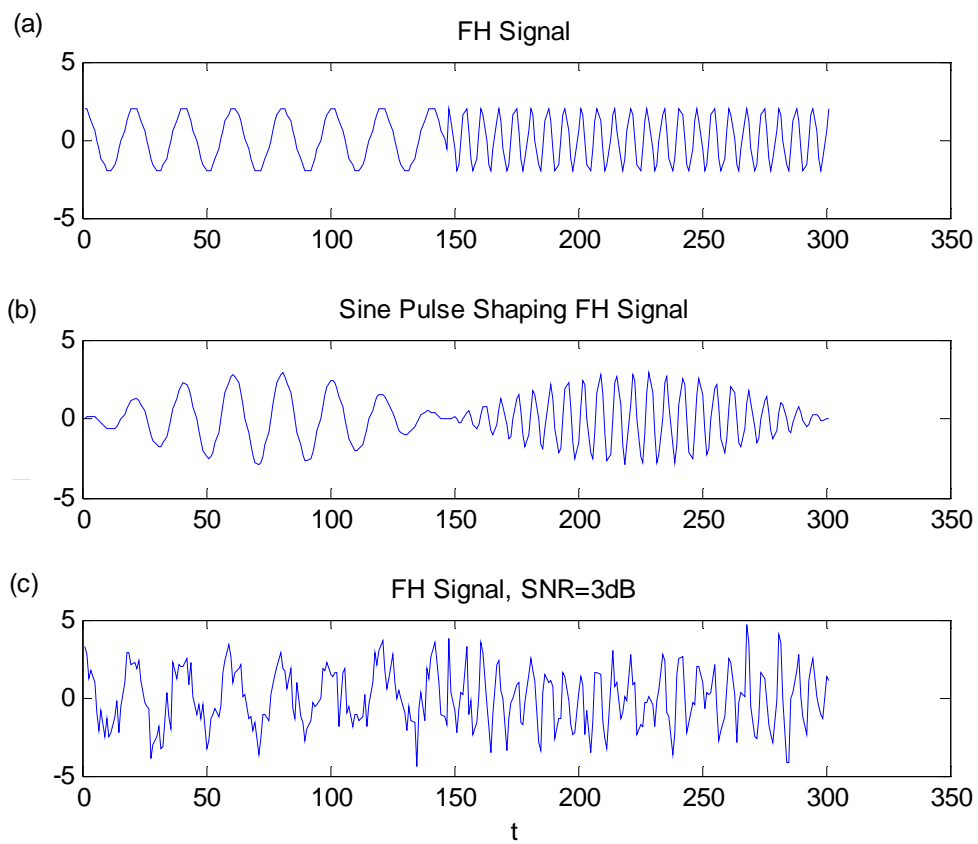


Figure 26. One-Hop FH Signal. (a) Basic FH Signal (no pulse shaping). (b) FH Signal with Sine Pulse-Shaping. (c) Basic FH Signal, SNR=3 dB.

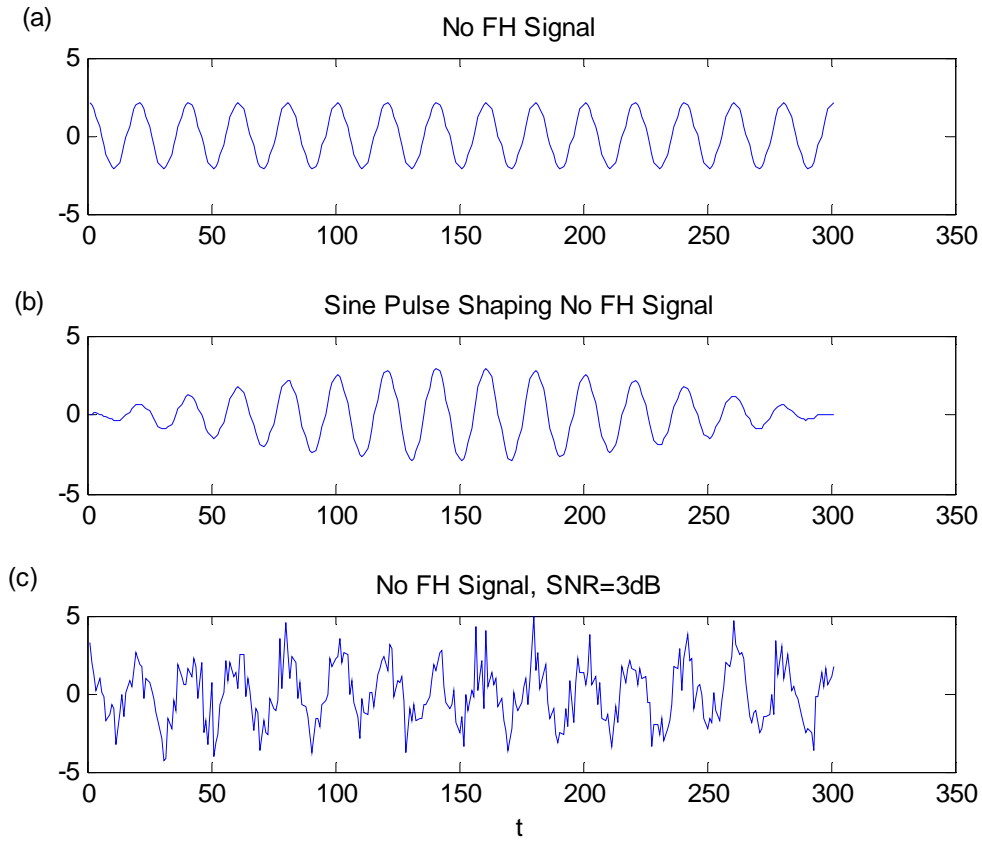


Figure 27. No-Hop FH signal. Basic FH Signal (no pulse shaping). (b) FH Signal with Sine Pulse Shaping. (c) Basic FH Signal, SNR=3dB.

The basic FH scheme considered in this work has rectangular symbol pulses, which may result in strong discontinuous signal between symbols. For example, the one-hop FH signal $x(t)$ within a time frame has for definition:

$$x(t) = \cos\left(2\pi f_n \times \frac{T_n}{f_s} t\right), \quad n=1,2, \quad (6.1)$$

where f_s is the sampling frequency, f_1 and f_2 are the symbol frequencies, and T_1 and T_2 are the symbol pulse signal durations, respectively. For example, for a FH signal sampling frequency $f_s = 150\text{Hz}$, with first signal frequency $f_1 = 15\text{Hz}$, second signal frequency $f_2 = 45\text{Hz}$ and signal duration $T_2 = 1\text{ sec}$, the

total number of samples in the FH frame is equal to $(T_1 + T_2) \times f_s = 2 \times 150 = 300$ and the frequency change occurs at sample $t_{hop} = T_1 \times f_s = 1 \times 150 = 150$.

Note that basic FH signals have high spectral sidelobes which may be reduced by applying pulse shaping. Half sine wave pulse-shaped FH signals have smaller discontinuities between frequency hops, resulting in sidelobes with energy 50 dB lower those observed in the basic FH scheme, as illustrated in Figure 28.

Thus, we also considered FH signals with pulse-shaping and investigated how pulse shaping affects our estimation algorithm. We introduced pulse shaping to the FH by multiplying basic rectangular symbol pulses with a half sine wave function. As a result, the pulse-shaped FH signal $x_{PS}(t)$ is given by:

$$x_{PS}(t) = \cos\left(2\pi f_n \times \frac{T_n}{f_s} t\right) \cdot \sin\left(\pi \times \frac{T_n}{f_s} t\right), \quad n=1,2. \quad (6.2)$$

Figure 26 (b) and Figure 27 (b) show that the rectangular-truncated basic FH signal is smoothed evenly by the half sine function going from $\sin(0)$ to $\sin(\pi)$.

In both cases, the frequency jump may be very hard to see in the time domain when noise is present, as illustrated in Figure 26 above, where the true frequency jump is at time $t=150$.

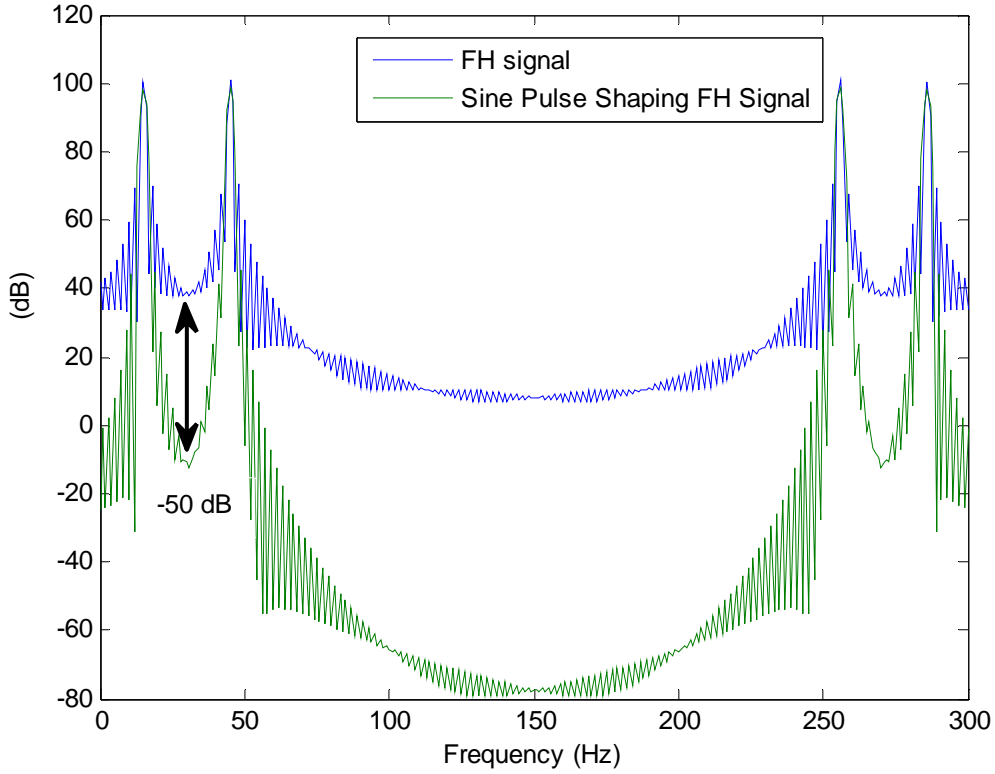


Figure 28. Frequency Response of Basic FH Signal vs. Sine Pulse-Shaped FH Signal.

In our work, we constrain the potential true hop not to be located towards either end of the signal frame. Note we added this constraint for convenience only. In practical applications, this issue could be addressed by overlapping successive time window frames, so that the algorithm has multiple looks of the same FH hop section. This constraint was added as the TCF phase matrix has large discontinuities at its outside boundaries that are removed by applying a mask in the first stage of the algorithm. However, such discontinuities could also hide discontinuities due to a frequency hop when the true hop location is located close to either end of the signal frame and be removed by the mask. Specific details regarding the mask implementation are given in Section VI.A.2.f.

b. Signal Hilbert Transformation

Overdyk [3 pp. 47-51] showed that undesirable cross terms present in the phase of the TCF derived from the real FH signal may be avoided when computing the TCF of the analytic signal derived from the real FH signal. The Hilbert transform is used to transform the real FH signal into its analytic version and has the following transfer function [after 12].

$$H_{hb}(\omega) = \begin{cases} -i = e^{\frac{-i\pi}{2}} & , \text{ for } \omega > 0 \\ 0 & , \text{ for } \omega = 0 \\ i = e^{\frac{i\pi}{2}} & , \text{ for } \omega < 0 \end{cases} \quad (6.3)$$

c. Temporal Correlation Function (TCF) Generation

First, the TCF is computed over a time frame using the analytical signal derived using the Hilbert transform, following Equation (6.3). Next, the phase information is extracted by computing the phase along the time axis (while keeping the lag τ constant).

d. TCF Phase Extraction

Figure 29 plots the TCF phase obtained for a one-hop FH noisy signal with hopping time at sample $t_{hop}=150$ for SNR equal to 9 dB. Note the three visible TCF phase regions and the tip of the cross-term phase region pointing at the position of the hopping time t_{hop} .

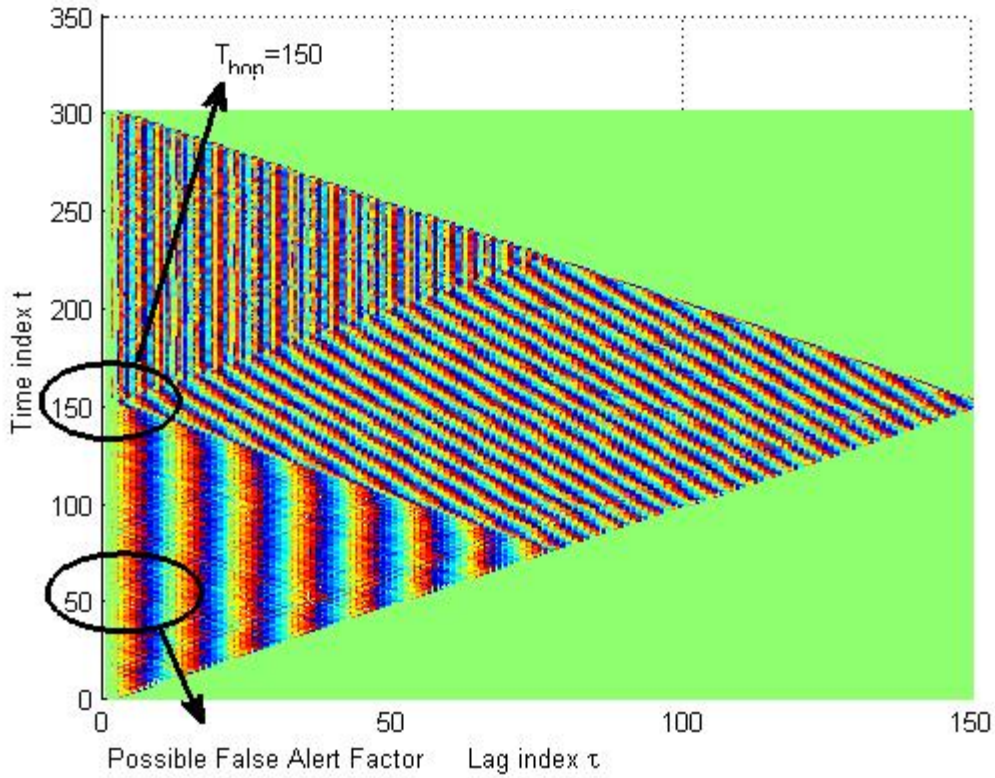


Figure 29. TCF Phase Plot with SNR=9 dB.

2. TCF Phase Region Edges Enhancement

Discontinuities between the three TCF regions phase components are clearly visible in medium to high SNR levels. However, further processing is needed to extract them in medium to low SNR levels. This section describes the various steps taken in Phase 2 for their enhancements.

a. TCF Phase Term Unwrapping Along the Time Axis t

The raw phase plot clearly shows the position of the hopping time in high SNR levels. However, the TCF phase information becomes degraded when the SNR level decreases and boundaries between the three TCF phase regions blurred. In such a case, unwrapping the TCF phase term, as defined

earlier in Chapter III.A, along the time axis “t” is applied to emphasize discontinuities between TCF cross-term and auto-term phase regions.

b. Applying Median Filtering to the Unwrapped TCF Phase Along the Time Axis t (filter length 15)

Next, we apply a median filter to the unwrapped TCF phase along the time axis t (while keeping the variable τ constant) to remove noise outliers while preserving long term trends in the TCF phase. The median filter described earlier in Chapter III.C, has been used extensively in signal processing for such a purpose and its length equal to 15 was selected by trial and error.

c. Differentiating the Unwrap TCF Phase Along the Time Axis t

Next, we differentiate the resulting TCF phase along the time axis to emphasize the discontinuities present at the boundaries of the three TCF phase regions. The resulting TCF phase expressed as a function of t becomes a step. Figure 30 presents the result obtained after unwrapping, applying the median filter of length 15, and differentiating the TCF phase shown previously in Figure 29. Note the region referred to as $TCF_{12}(t, \tau)$ is now a high-level plateau in the figure, while regions referred to as $TCF_1(t, \tau)$ and $TCF_2(t, \tau)$ are now low-level plateaus.

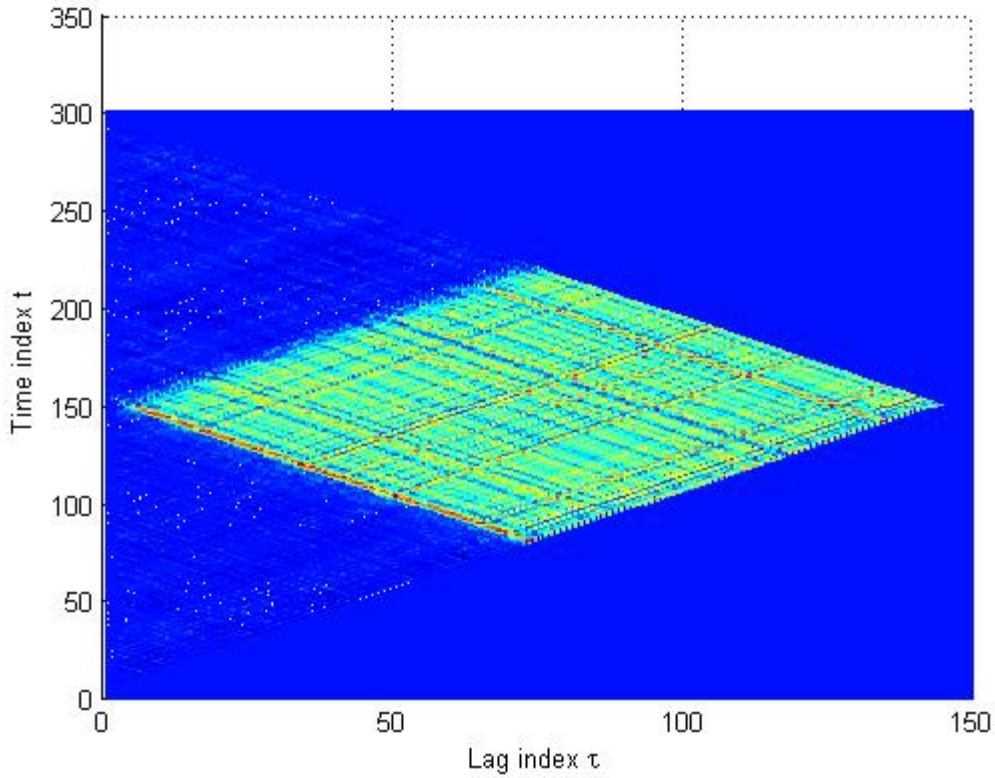


Figure 30. Differentiation Operation Applied to Unwrapped TCF Phase.

d. Applying Median Filtering to the Differentiated Phase Along the Time Axis t (filter length 30)

Figure 30 shows that small noisy discontinuities are still contained in the TCF phase after differentiation. A second stage median filter of length 30 suppresses the small noisy spikes, as illustrated in Figure 31. The resulting TCF phase is used to extract the hopping time t_{hop} information. Note that the median filters are responsible for the disappearance of the TCF phase discontinuities for values of τ below 10, as shown in Figure 31 (“missing tip” annotation). However, discontinuities present for larger values of τ are sufficient to extract the hopping time information.

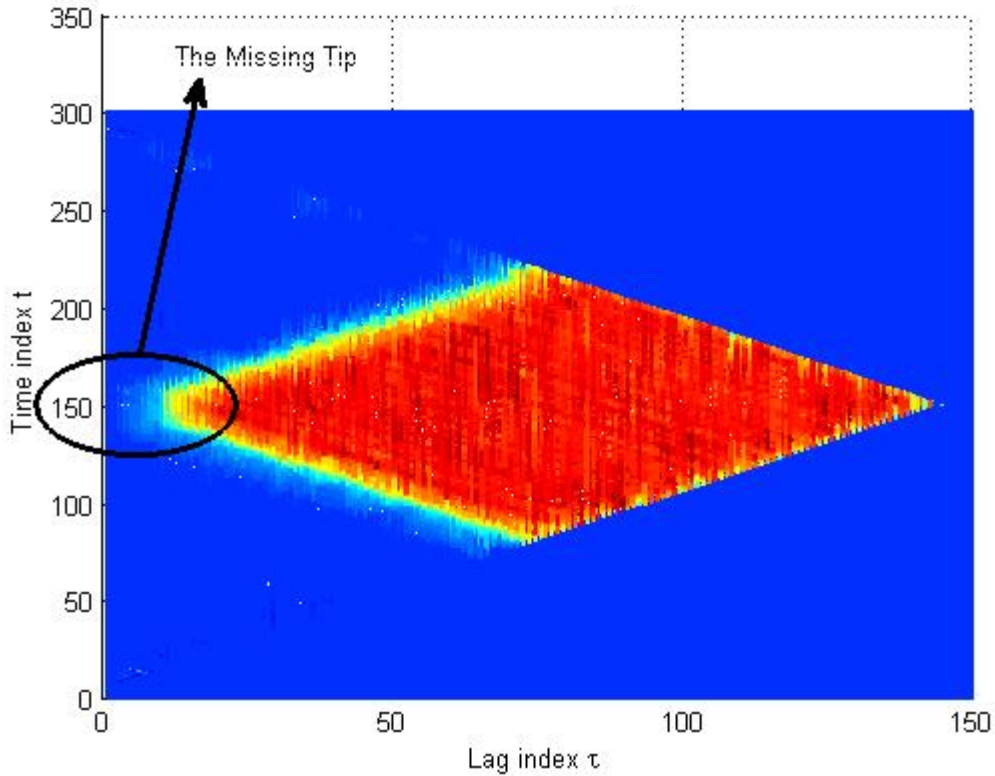


Figure 31. Median Filtering of the Differentiated TCF Phase Along the Time Axis t , Median Filter Length Equal to 30.

e. Computing the Wavelet Transform Along the Time Axis t

Next, the Wavelet transform is applied to the resulting unwrapped and differentiated TCF phase along the time axis to emphasize the signal discontinuities along that axis. Note that only the first third of the TCF phase along the τ axis is processed via the wavelet transform as the hopping location information may be recovered from that range. Two different wavelet transform approaches were considered in this work; a one-level discrete wavelet transform (DWT) using Haar wavelets, and the continuous wavelet transform. Note the MATLAB-based DWT implementation includes a down-sampling operation, which gets reversed by up-sampling the results by a factor of two. This last up-sampling step was added for convenience purposes only, to keep the same number of samples as those in the original TCF phase expression.

Figure 32 shows the results obtained by applying the one-level DWT to results shown in Figure 31.

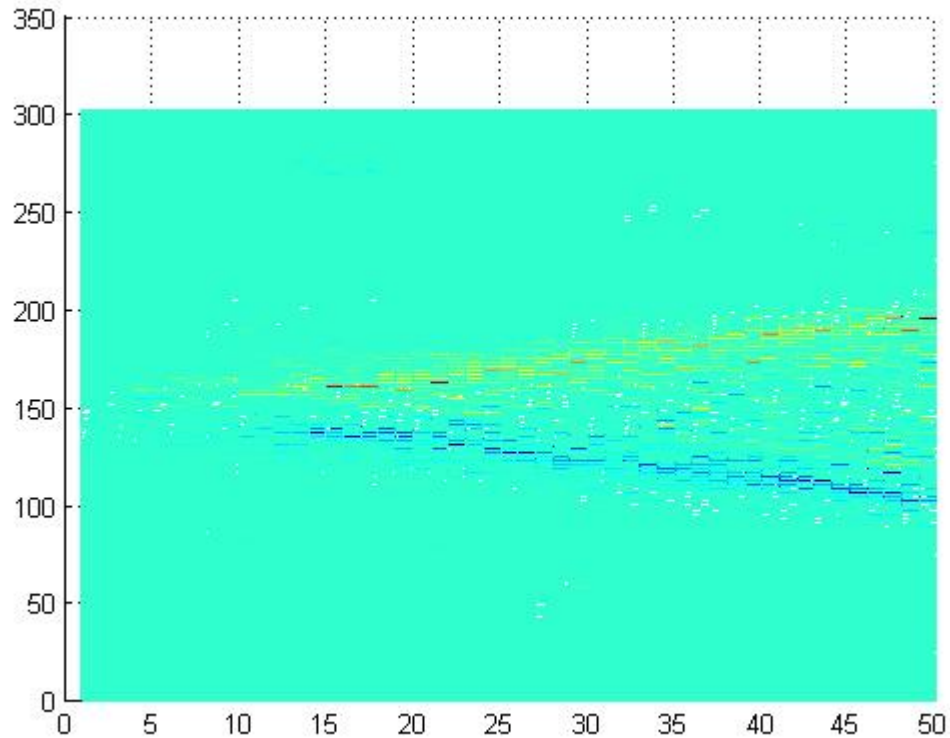


Figure 32. DWT Detail Coefficients Obtained after Applying the One-Level DWT Transform (Haar wavelets) to the TCF Phase Shown in Figure 31.

f. Removing TCF Boundary Edges

Applying the continuous or discrete wavelet transform produces discontinuities at the TCF phase outside boundaries that may be significantly larger than those observed between the TCF regions. Thus, a triangular mask is applied to the outside boundaries regions to remove these discontinuities which would overwhelm the discontinuities of interest contained within the TCF phase. The mask is with the same size as that of the TCF phase, and is designed to zero out the 15 values found along the edges of the TCF phase plane.

g. Threshold Wavelet Coefficients

The wavelet transform contains many small value coefficients due to noise contributions. Coefficients with small magnitude are not representative of the boundaries between the TCF regions and zeroed out to clean up the image. In this work, we only keep WT coefficients with magnitude above 40% of the coefficient with largest magnitude.

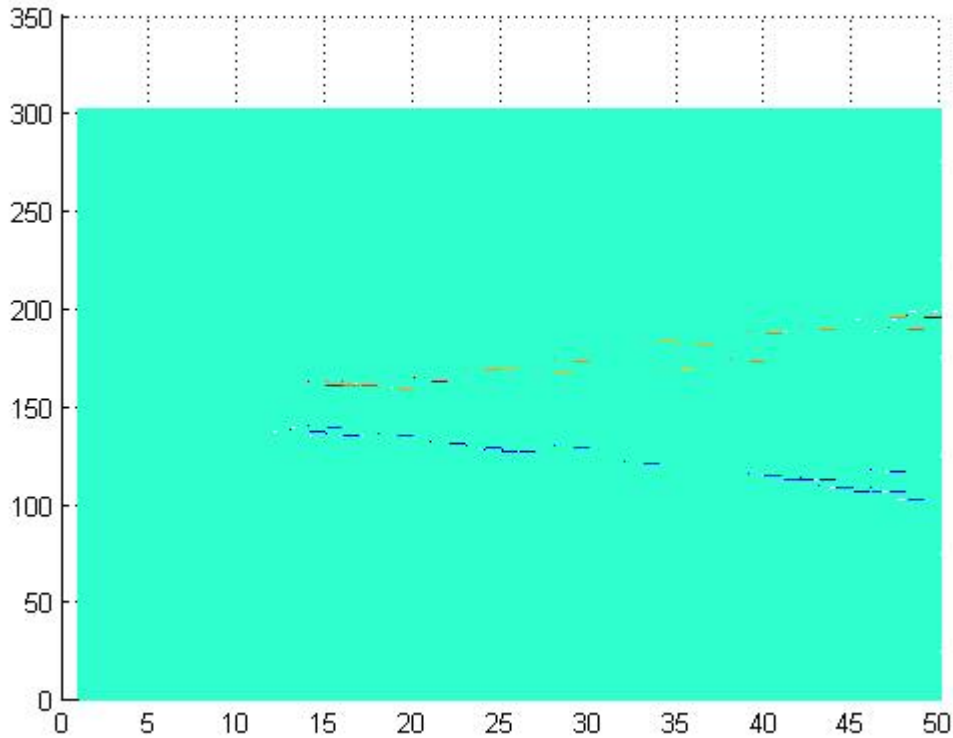


Figure 33. Figure 32 after Thresholding DWT Coefficients; Threshold Equal to 40% of the Coefficient with Largest Magnitude.

3. Binary Image Processing and Estimation

Phase 3 follows an image processing approach to the detection of hopping time location(s). Morphological tools are used to extract edges from the processed TCF phase information obtained after wavelet transformation of the TCF phase expression.

a. Edge Detection Operation

First, we apply an edge detection algorithm to extract the TCF phase region boundaries from the wavelet transformed TCF phase obtained in Stage 2. The function used in our implementation is the MATLAB function “edge” which finds edges using the Sobel operator [13]. Figure 34 shows the original plot obtained after applying the edge detection function. Note the gray scale image has been transformed into a binary black-and-white image, and the two $\pm 45^\circ$ lines that intersect at the location t_{hop} along the y-axis.

b. Erosion Operation Using a Diagonal Alignment Mask

Initial simulations showed that resulting image usually contains what we refer to as “noisy pixel” contributions, i.e., small broken line segments and isolated pixels due to noise distortions, as shown in Figure 34 (2-bit erosion figure) and Figure 23 (3-bit erosion figure). Thus, we added an erosion step in an effort to remove these noisy pixel contributions. We applied two diagonal masks, one with $+45^\circ$ and the second one with -45° orientations to remove such noisy contributions. We considered masks with 2- and 3-bit size and compared the resulting hopping time detection performances obtained with each. Results showed the 3-bit mask may be more successful at removing isolated segments than the 2-bit mask is, as shown in Figure 34 and Figure 23. However, they also indicate that the 3-bit mask may end up removing too much of the line detail, making it harder to accurately estimate the hopping time, as simulations showed that the 2-bit mask results in better detection performances than those obtained with the 3-bit mask.

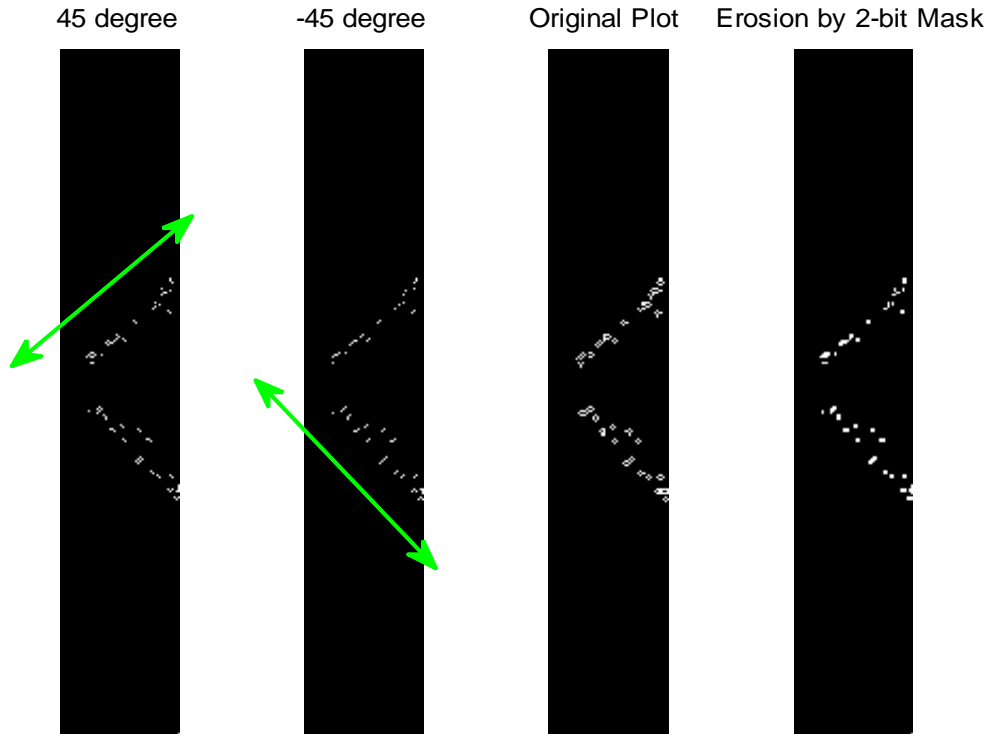


Figure 34. 2-bit Mask Erosion Operations with 45° and -45° Orientations.

c. Hopping Time Index Estimation Using the Hough Transform

Next, the Hough transform is applied to the processed image using the MATLAB function “hough”. Note the user needs to indicate the maximum number of lines to be detected in the image by the MATLAB function “houghpeaks”, which was selected to be up to six in our work. This specific number was selected as we restricted our study to scenarios where we have at most one hop in each collected frame. Figure 35 below shows six peaks in the Hough transform plane, each corresponding to an estimated line equation represented in the Hough plane by its ρ and θ parameters.

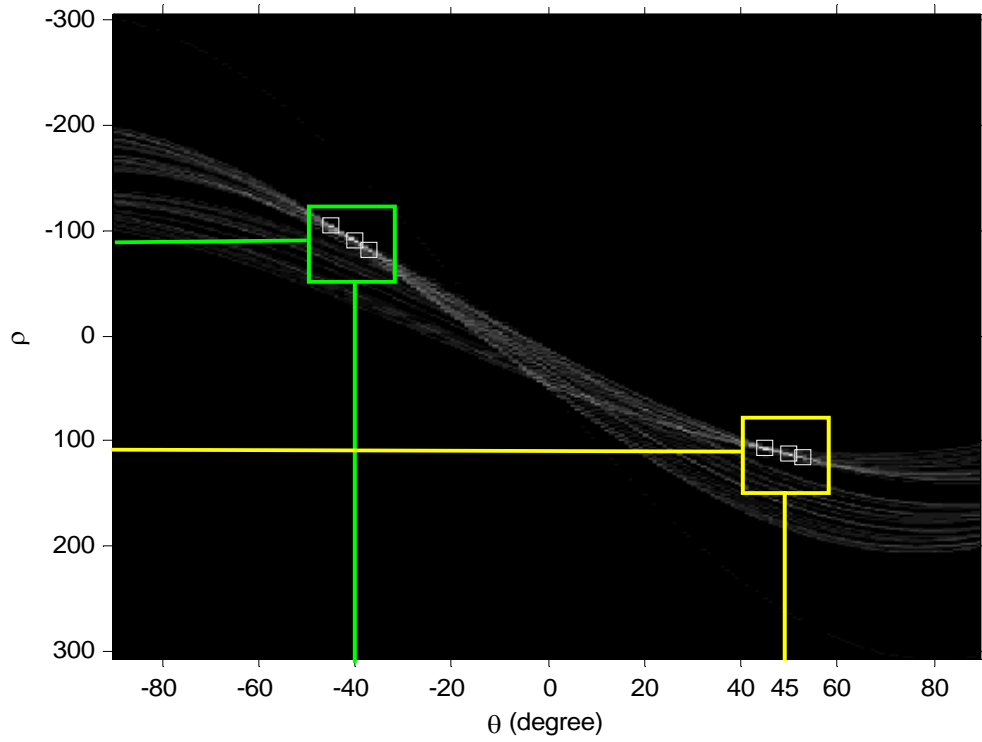


Figure 35. Hough Transform Plot with 6 Peaks.

Recall that the lines of interest in the TCF plane are expected to have $\pm 45^\circ$ orientations. Thus, we discard lines not located close enough to these orientations, and estimate t_{hop} from the remaining line parameters using Equation (5.12).

Peak Value no.	1	2	3	4	5	6
θ°	50	45	-40	-45	-37	53
ρ	111.3651	106.3487	-90.2961	-104.342	-81.2664	114.375
Estimated Hopping Time	145.3769	150.3998	140.4757	147.562	Discarded	
Median Value Hopping Time	146					

Table 2. Hopping Time Evaluation Process Using Hough Transform Parameters.

Note that allowing for six lines in the TCF phase processed image results in six possible hopping time locations. Thus the final hopping time location is identified by selecting the median point among possible values once those judged too far away have been discarded.

B. SIMULATION RESULTS

The detection scheme considered in this study requires the user to select the following parameters: median filter lengths, wavelet function type in Stage 2; erosion mask size, and hopping time location tolerance level in Stage 3. This section presents detection performance results obtained in terms of these parameters.

1. Signal Generation Specifics

Five hundred trials were run per simulation to compute performance results shown in Figure 36 to 50. In each trial, the signal has an even chance to contain one-hop or no-hop. Therefore, each simulation run contains about 250 no-hop and one-hop signals. Note we also ran simulations with 1000 trials, which led to similar results as those obtained for 500 trials/runs. As a result, all performance results included in this document use 500 trials/run.

All signals were generated with sampling frequency $F_s=128$ Hz and total signal length $T_s=2$ (s), resulting in 256 samples/signal. Recall, that we only consider FH signals with at most one hop per frame in this work. Next, we describe the constraints applied to the FH signal snippets generated.

a. One-Hop FH Signal Case

The first signal frequency f_1 is randomly selected between $0.15F_s$ and $0.25F_s$, i.e., 19.2 Hz and 32 Hz, and the frequency hopping location t_{hop} is uniformly distributed between 0.6 and 1.4 seconds, i.e., between samples 153 and 358.

We constrain t_{hop} to be at least 10% away from both signal frame ends to insure the hopping time location information is not removed when the TCF mask is applied, as described in Section VI.A.2.f.

We assign a minimum hopping frequency jump equal to $0.2F_s=25.6$ Hz i.e., the second signal frequency f_2 is set at: $f_2 = f_1 + 0.2F_s = f_1 + 25.6$ Hz. Thus, the duration of the FH signal with frequency f_2 is $T_s - t_{hop}$.

b. No-Hop Signal Case

The no-hop signal of duration $T_s=2s$ contains one frequency only in the signal frame. The frequency is chosen randomly between $0.15F_s$ and $0.25F_s$, i.e., between 19.2 Hz and 32 Hz, using the same procedure as that followed with the first frequency selection in the one-hop signal case.

c. Pulse Shaped FH Signal

The pulse shaped FH signal is computed by applying a half sine waveform to the basic FH signal in each interval with constant frequency, following the derivation given in Equation (6.2).

2. Performance Results

Each simulation run has 500 trials where each signal is generated to contain at most one hop within the collection frame. The signals are imbedded in additive white Gaussian noise in SNR levels between -6 dB to 21 dB in 3 dB increments.

a. Detection Accuracy Performance Results

Overdyk derived statistics for the accuracy of estimated hopping time locations in his earlier work [3 pp. 70], and similar statistics are computed here for comparison purposes. Note that noise distortions and processing steps are both responsible for introducing some inaccuracy in estimated hopping time

locations. As a result, detection performance results are given in terms of specific hopping time accuracy levels, and a hopping time location is said to be accurately estimated when it falls within the selected tolerance. For example, using a 5% tolerance level, the estimated t_{hop} time has to be within at most 5% away from the true hopping time location. Thus, for a frame size equal to 256 and a 5% tolerance level, the estimated hopping time location is considered to be accurately estimated when it is located within $256 \times 0.05 \cong 12$ sample points from the true hopping time location. Figure 36 shows hopping time detection performance results for various tolerance levels and SNR levels between -3dB to 21dB. The following three overall comments can be made:

- Detection performance results obtained for a 0% tolerance level are poor. This behavior is the result of the various filtering and image processing steps contained in Stages 2 and 3 of the algorithm which introduce some small errors in the hopping time location. However, detection performance results significantly increase for SNR levels between 0 and 21dB when a small 5% tolerance level is introduced in the final detection stage.
- The results obtained for tolerance levels between 20% to 40% are very similar. Therefore all detection performance results presented later in this work use a 20% tolerance level.
- The algorithm provides reliable detection for SNR level above 3dB. Performance results degrade significantly for SNR levels below 3dB, and the detection scheme, as proposed in this work, may not be very useful in environments below 3dB.

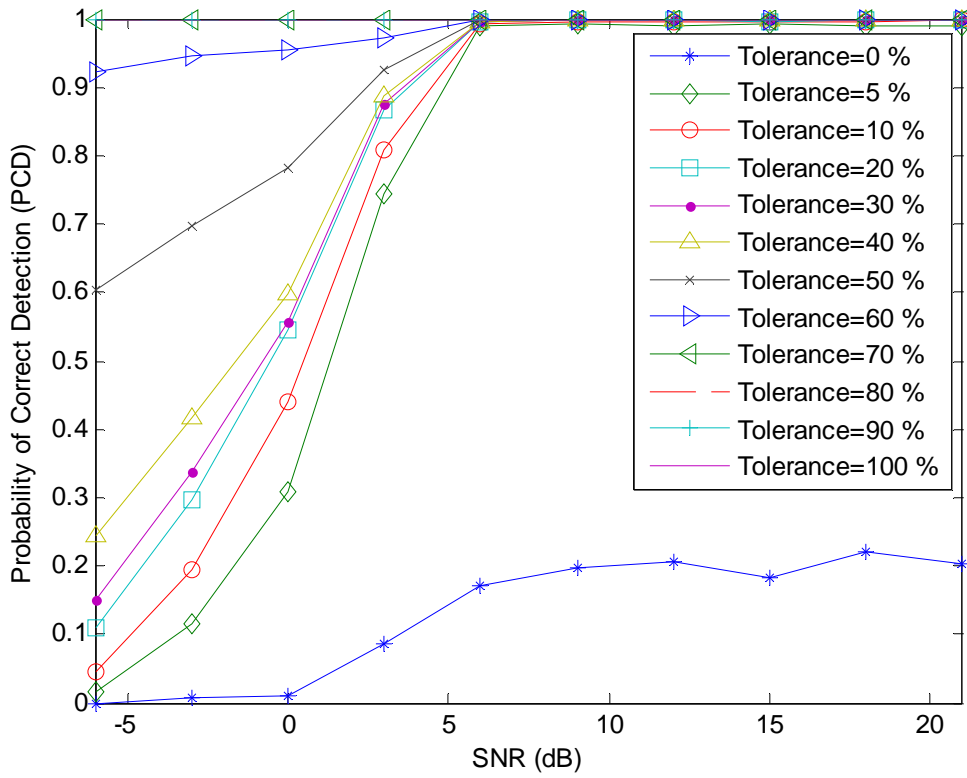


Figure 36. One-Hop Detection Performance Results for Different Accuracy Tolerance Levels, SNR Levels between -6db to 21dB, Frame Size=256.

b. Median Filter Length

The final detection algorithm has two median filters included in Stage 2; one before the TCF phase differentiation step and one following it. These two filters are added to remove small discontinuities in the traces, while preserving the long term trends. Figure 37 presents hop timing detection performance results obtained for various median filter length combinations, as a function of the SNR level for a 20% detection tolerance level. Results show the best overall performance is obtained when the two median filters' lengths equal 15 and 30, respectively.

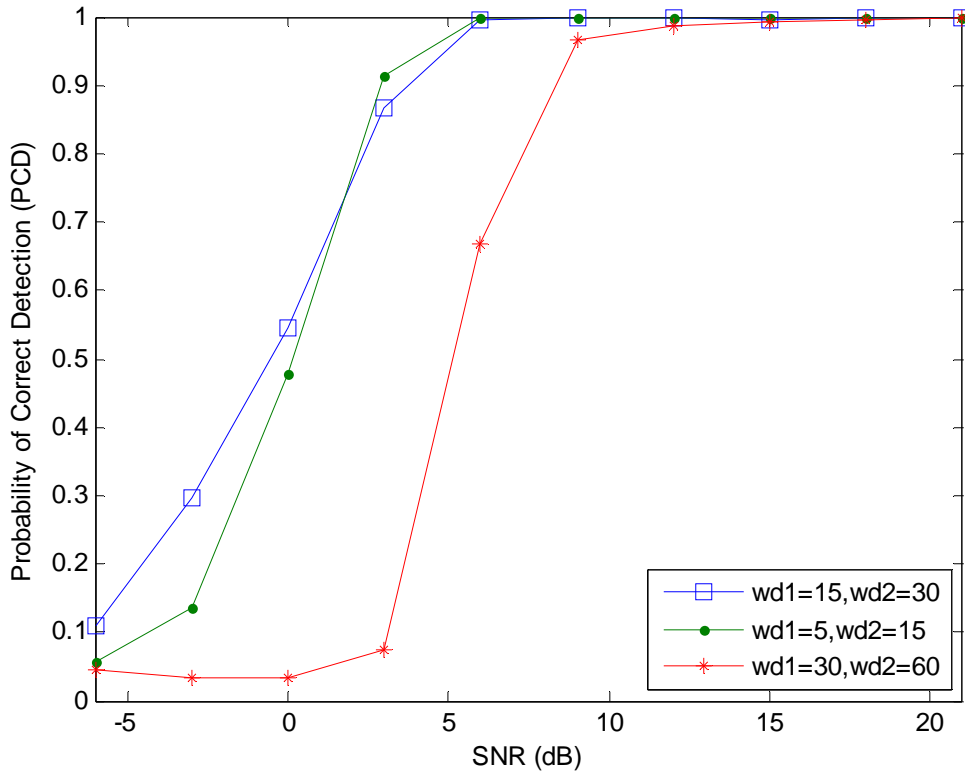


Figure 37. One-Hop Correct Detection Performance Results as a Function of the Median Filter Lengths; wd1: 1st Median Filter Length, wd2: 2nd Median Filter Length, 500 Trials per Simulation, SNR Levels Between -6dB to 21dB, 20% Tolerance Level.

Figure 38 presents detection performance results obtained for the no-hop FH signal case, for the same combination of median filter lengths as those presented in Figure 37. Results show best results are obtained for a combination of longer median filter lengths (lengths 30 and 60, respectively for first and second median filters) than those selected for the one-hop case. However, these lengths also lead to poor performances for the one-hop signal case.

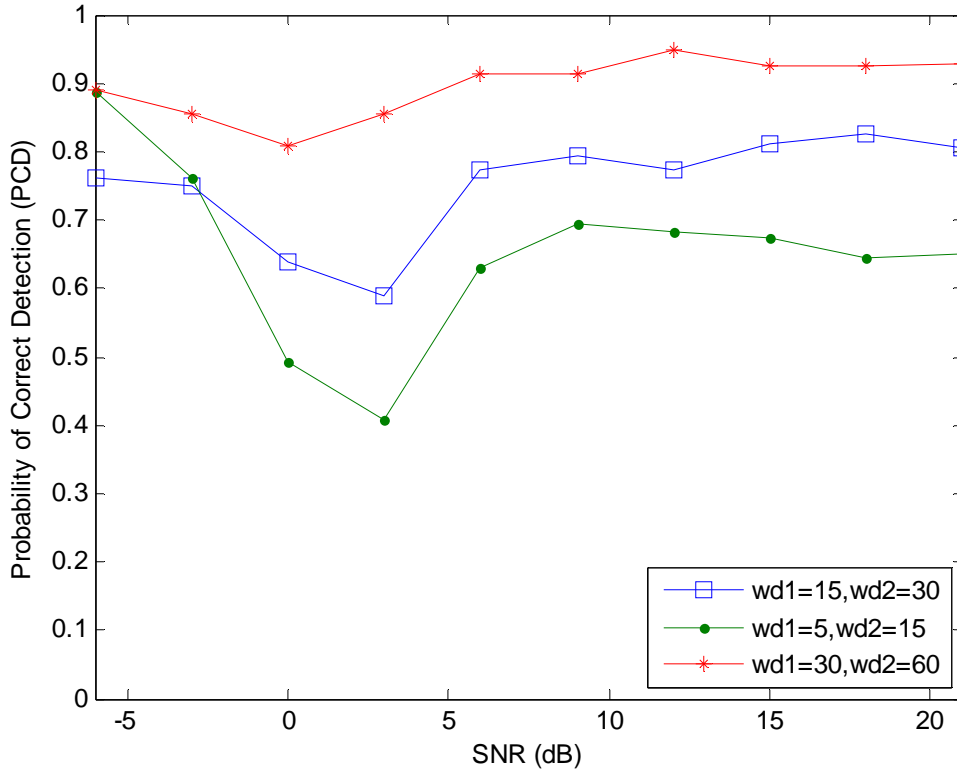


Figure 38. No-Hop Correct Detection Performance Results as a Function of the Median Filter Lengths; wd1: 1st Median Filter Length, wd2: 2nd Median Filter Length, 500 Trials per Simulation, SNR Levels Between -6dB to 21dB, 20% Tolerance Level.

c. *Pulse Shaped FH Signal*

Figure 39 and Figure 40 present one-hop and no-hop detection performance results obtained for the basic FH signal case and pulse shaped signal case, i.e., when no pulse shaping is applied to each symbol, and when half sine wave pulse shaping is applied. Results show detection performances degrade slightly when pulse shaping is introduced for SNR levels below 6dB. This behavior is the result of smaller TCF phase discontinuities at symbol ends due to the pulse shaping operation that decreases signal contributions at these locations.

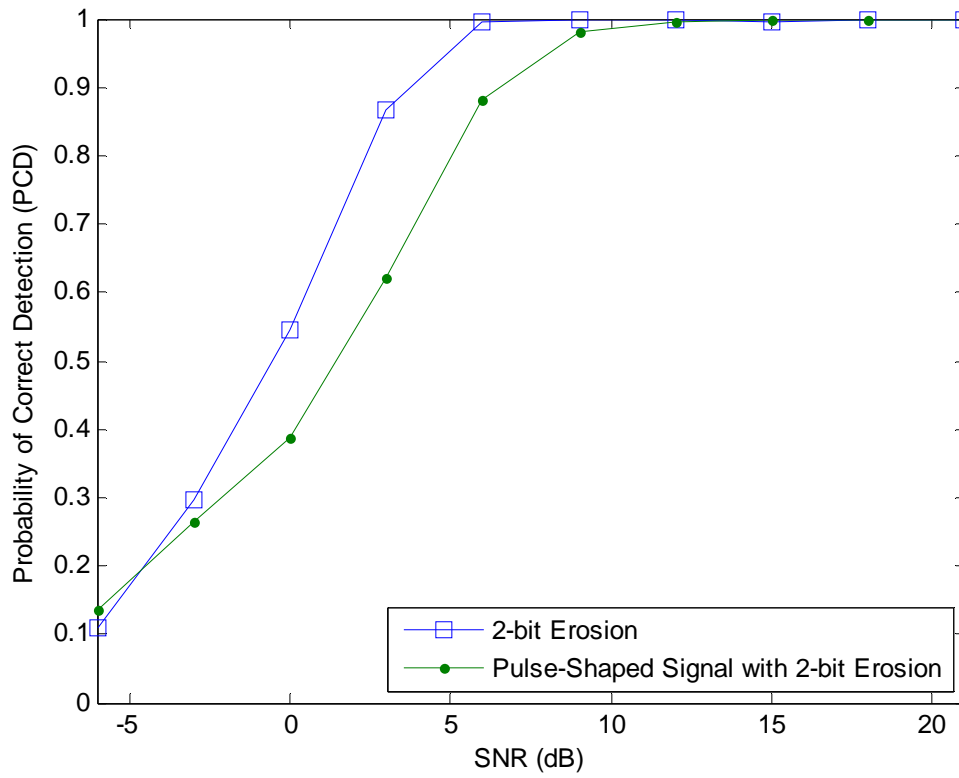


Figure 39. One-Hop Detection Performance Results for Basic FH Signal and Half Sine Wave Pulse Shaped FH Signal; 20% Tolerance Level, SNR Levels Between -6db to 21dB, Frame Size=256.

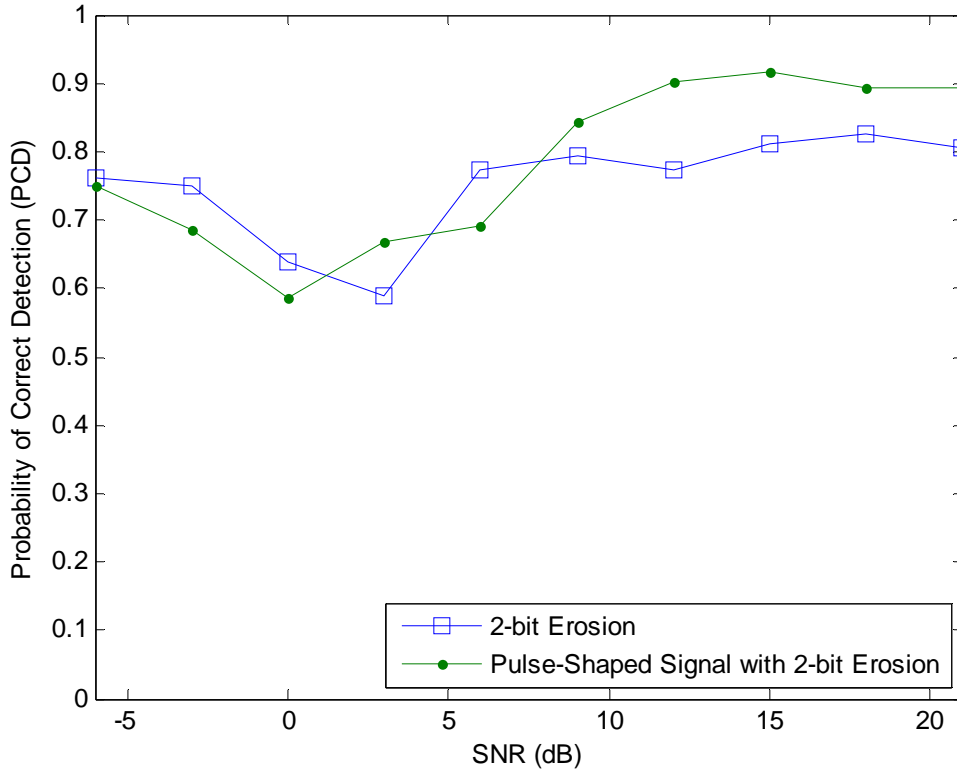


Figure 40. No-Hop Detection Performance Results for Basic FH Signal and Half Sine Wave Pulse Shaped FH Signal; 20% Tolerance Level, SNR Levels between -6db to 21dB, Frame Size=256.

d. No-Hop Signal Decision Using TCF Phase Variance Information

Recall that we introduced in Chapter III.D a basic scheme designed to test whether the analysis frame contained a hop or not, by tracking changes in the TCF phase short-term variance within the frame before applying any phase unwrapping. This basic step is added in Stage 1 in this set of experiments. Figure 41 and Figure 42 present no-hop and one-hop detection results obtained with and without this step added in Stage 1. Results show that one-hop detection performances are identical with and without this step added. Thus, the stage 1 TCF phase variance tracking algorithm does not degrade one-hop signal detection performances. Results also show that no-hop detection performance

improves for SNR level above 3 dB with this step added in Stage 2 of the detection algorithm, and reaches 100% accuracy for SNR levels above 6 dB.

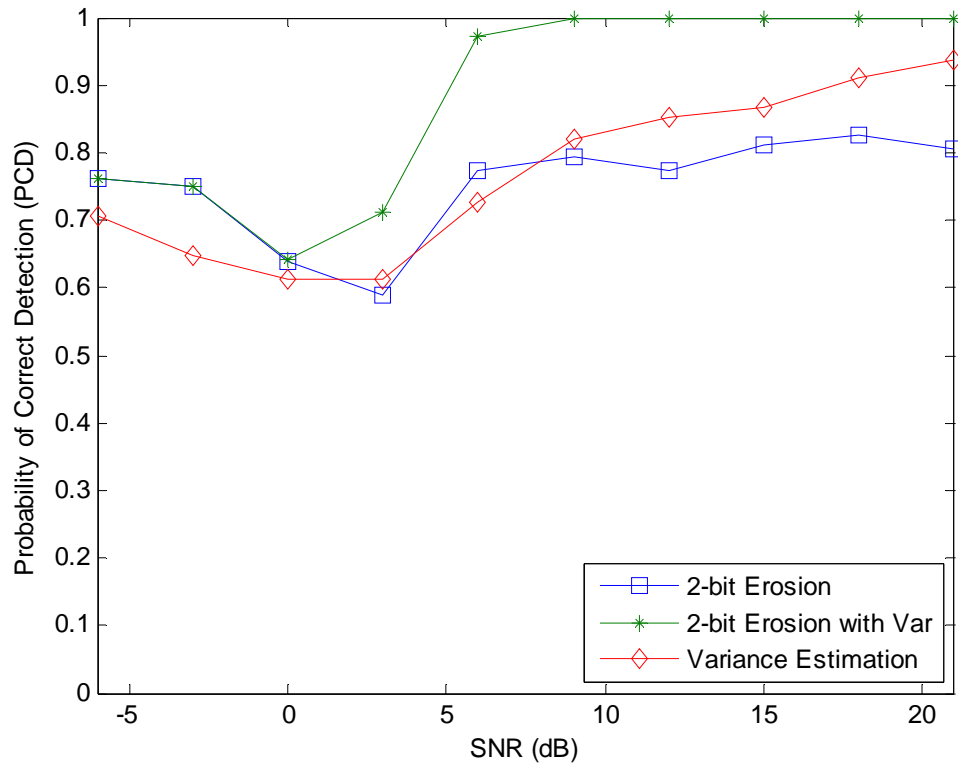


Figure 41. No-Hop Signal Estimation. (a) Basic No-Hop Decision (Blue Square), (b). Variance Tracking Added in Stage 1 Followed by No-Hop Decision (Green Dot), (c) Variance Tracking (Red Diamond).

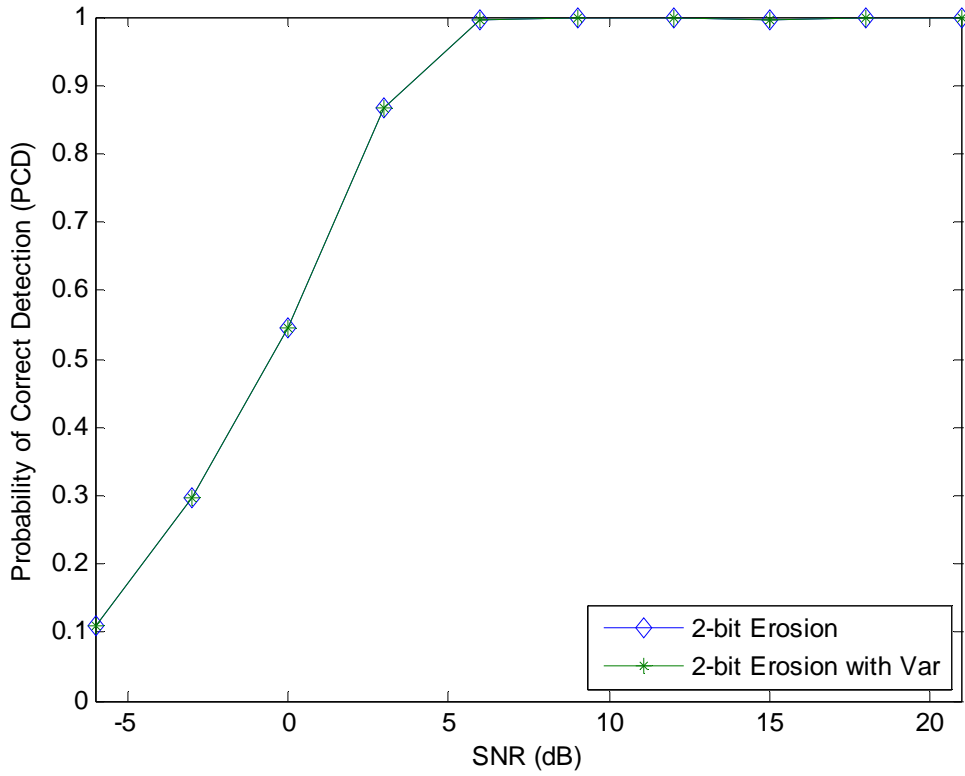


Figure 42. One-Hop Signal Estimation; (a) Basic One-Hop Estimation with 2-bit Erosion Mask (Blue Diamond), (b). Variance Tracking Added in Stage 1 Followed by One-Hop Estimation (Green Star), 20% Detection Tolerance Level.

e. *Morphological Erosion Step*

In Chapter V we discussed the morphological erosion step added in an effort to clean up the image before applying the Hough Transform and improve resulting detection performances. Figure 43 presents detection results obtained with and without the edge detection and morphological 2-bit erosion steps. When bypassing edge and morphological steps, the Hough transform is directly applied to a binary image obtained from the wavelet transform. In this scenario, all WT coefficients with magnitude larger than the threshold value are kept and transformed to 1, while others are set to zero. Results show one-hop

detection performances degrade for SNR levels below 6 dB showing morphological operations improve hopping detection performances in lower SNR environments.

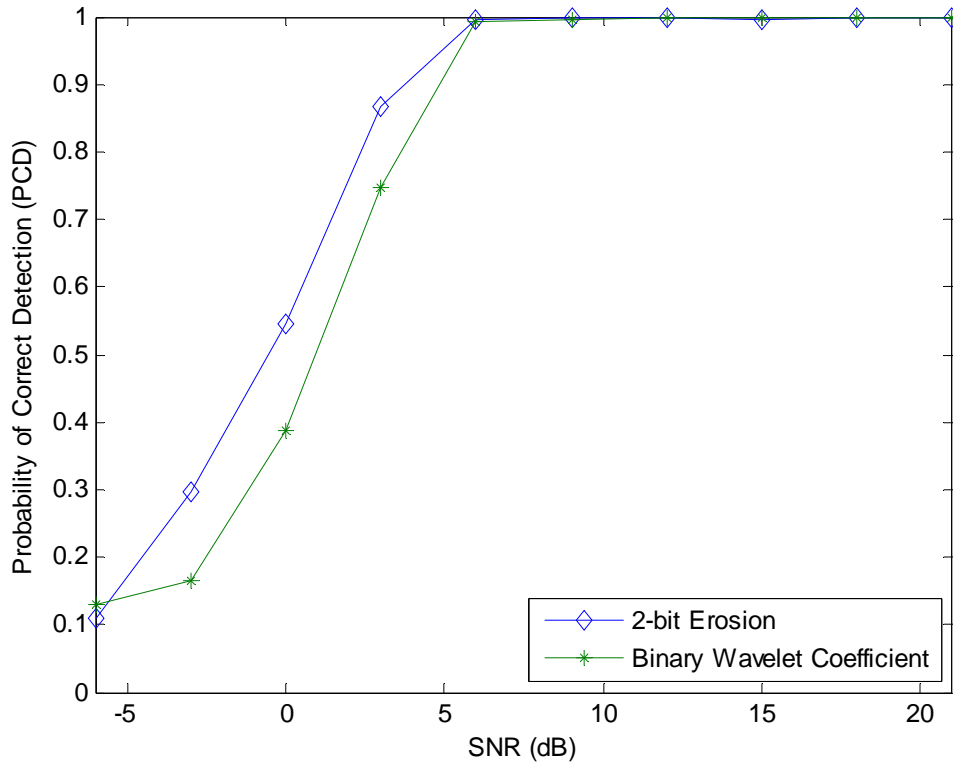


Figure 43. One-Hop Signal Estimation; (a) Basic One-Hop Estimation with 2-bit Erosion Mask (Blue Diamond), (b). Binary Thresholded Wavelet Transform Directly Applied to Hough Transform (Green Star).

Figure 44 presents no-hop decision performance results obtained with and without the edge detection and morphological 2-bit erosion steps applied in Stage 2. Results show no-hop decision results are only slightly better when edge and erosion steps are omitted in Stage 2. However, recall that these no-hop decision results do not take into account improvements added when adding the stage 1 variance block.

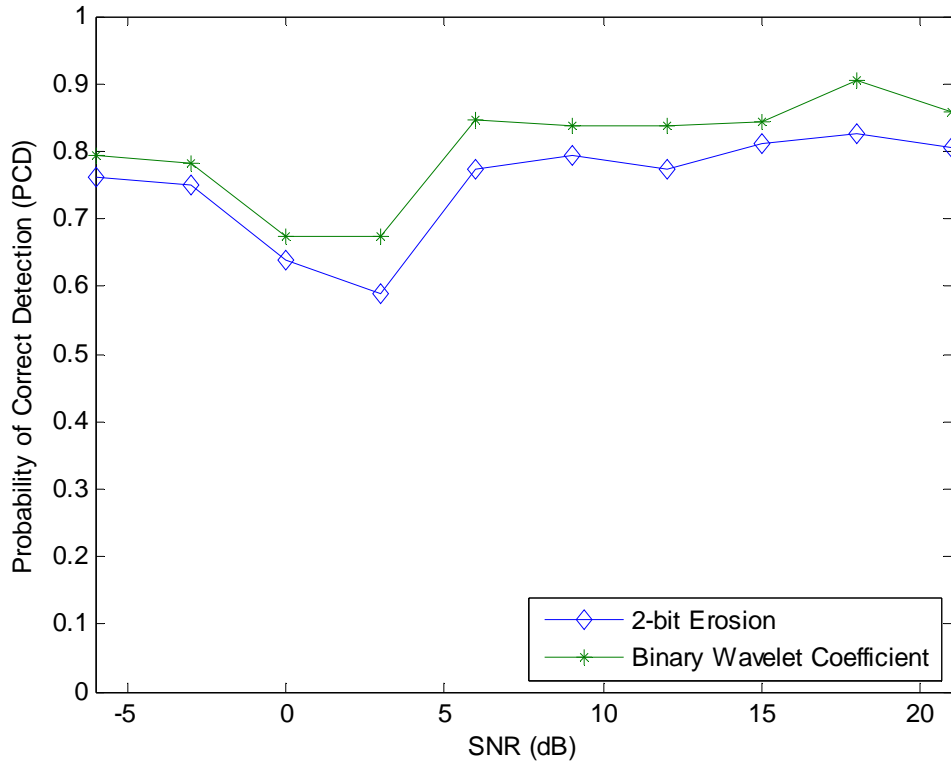


Figure 44. No-Hop Signal Estimation; (a) Basic One-Hop Estimation with 2-bit Erosion Mask (Blue Diamond), (b). Binary Thresholded Wavelet Coefficient before Hough Estimation (Green Star).

Figure 45 and Figure 46 show detection performance results obtained for one-hop and no-hop cases when applying 2-bit, 3-bit, or no erosion mask to the edge detected binary image. Results show that the 3-bit mask removed too much information and degraded one-hop detection performances for SNR levels between 0 to 6dB. Results also show the 2-bit erosion mask did not lead to significant performance improvements for the one-hop detection case.

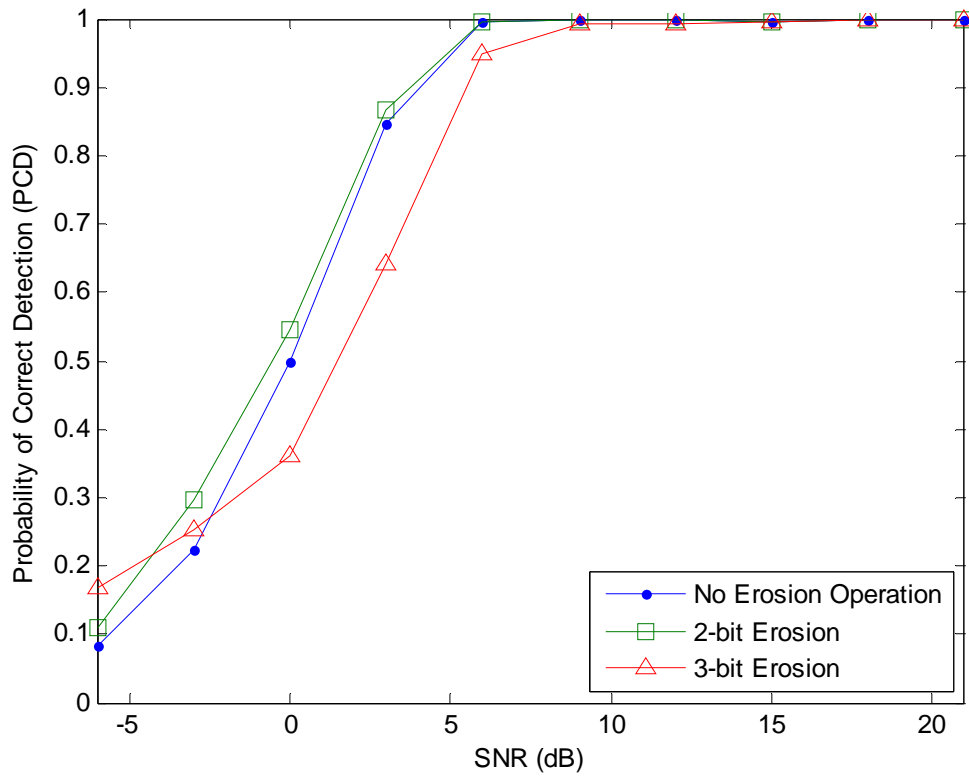


Figure 45. One-Hop Estimation Algorithm for Different Erosion Mask Lengths, (a) No Erosion Mask (Blue Dot), (b) 2-bit Erosion Mask (Green Square), (c) 3-bit Erosion Mask (Red Triangle).

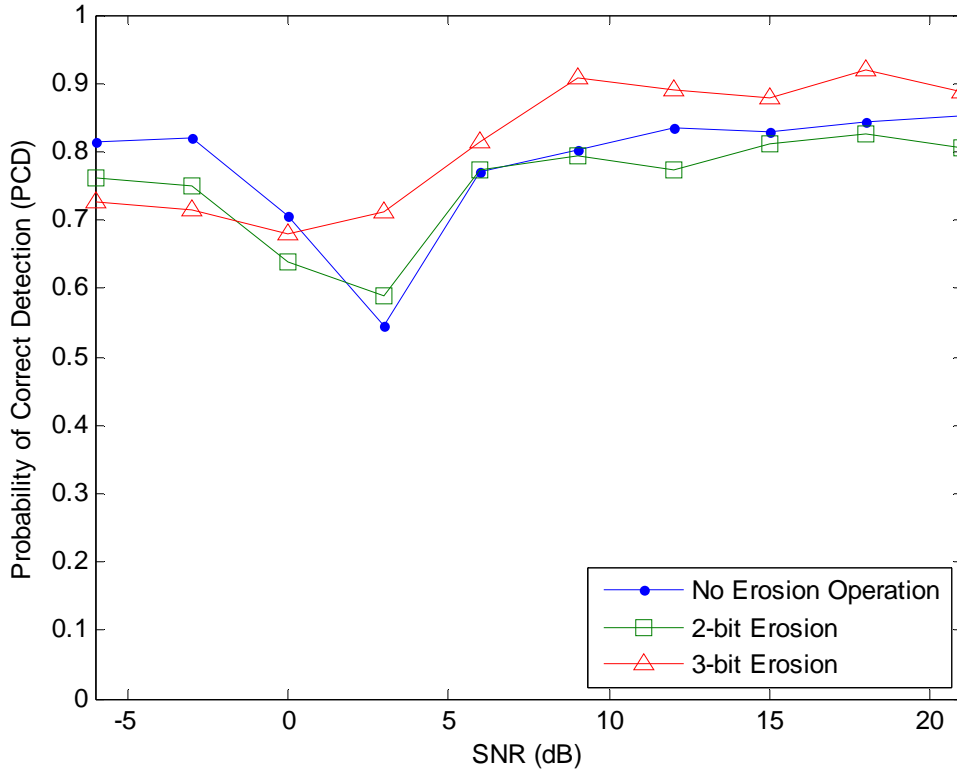


Figure 46. No-Hop Estimation Algorithm for Different Erosion Mask Lengths, (a) No Erosion Mask (Blue Dot), (b) 2-bit Erosion Mask (Green Square), (c) 3-bit Erosion Mask (Red Triangle).

f. Morphological Dilation Step After Erosion Operation

In this experiment, the dilation operation was applied after the erosion operation with the same alignment mask. Figure 47, and Figure 48 present one-hop detection and no-hop decision performance results for a 2- and 3-bit erosion operation followed by either 2-bit or 3-bit dilation steps applied afterwards. Results show adding a dilation step has no positive impact on performance.

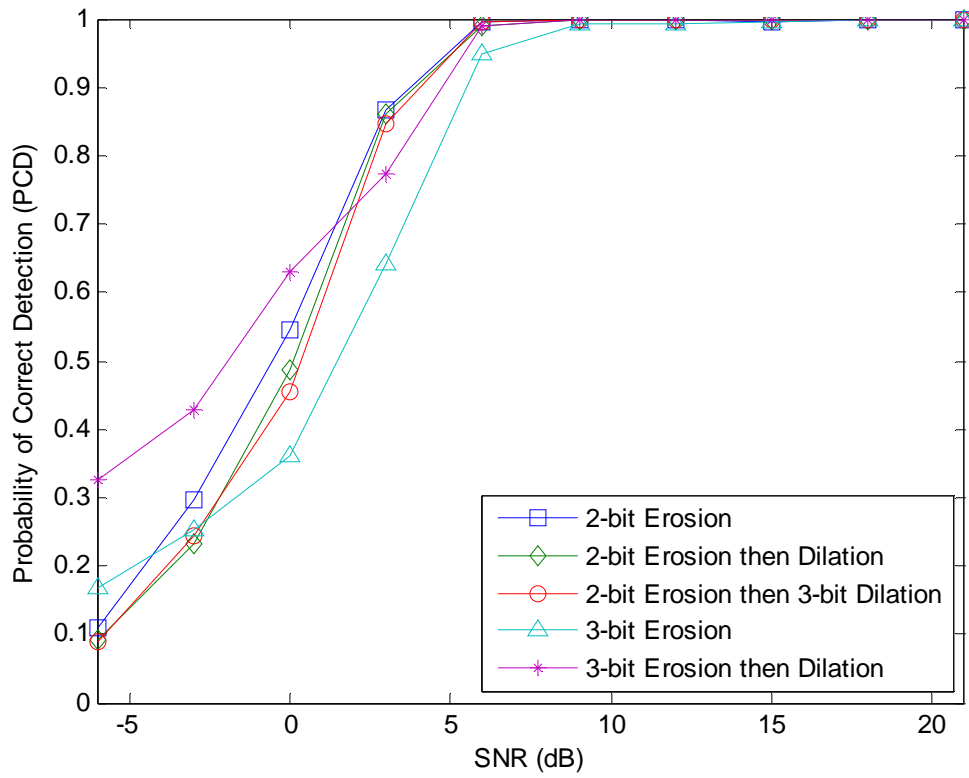


Figure 47. One-Hop Detection Performances for Various Combinations of Erosion and Dilation Masks, 2 and 3-bit Erosion Masks, 20% Hopping Time Tolerance Level.

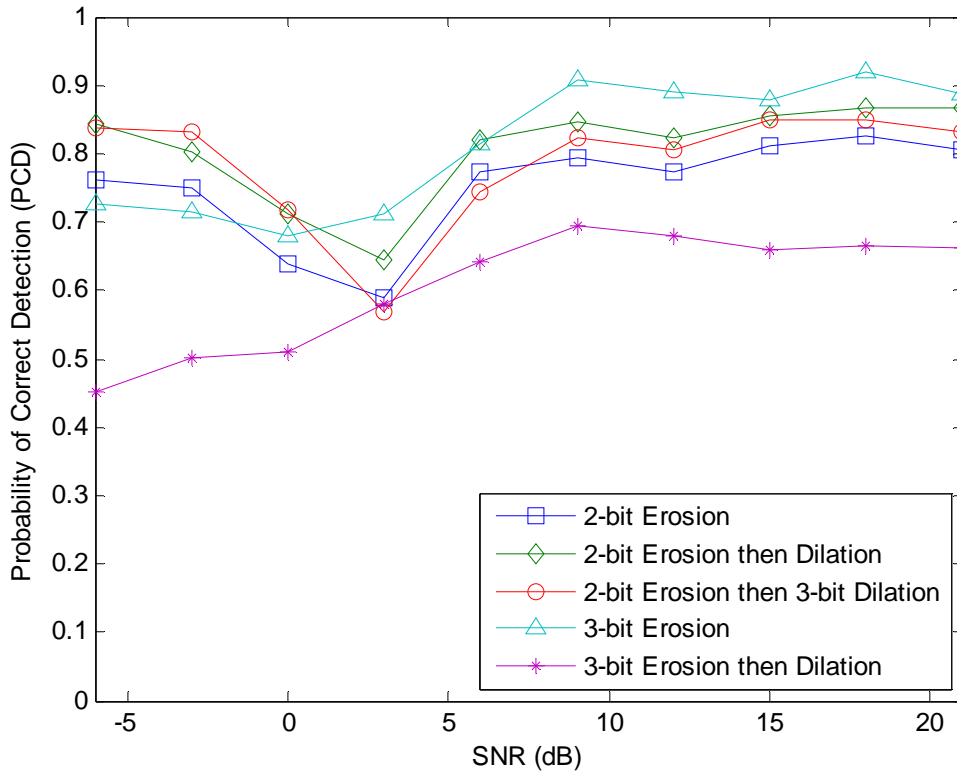


Figure 48. No-Hop Detection Performances for Various Combinations of Erosion and Dilation Masks, 2 and 3-bit Erosion Masks, 20% Hopping Time Tolerance Level.

g. Continuous Wavelet Transform (CWT) vs. Discrete Wavelet Transform (DWT) Performance

This section reports results obtained when using the Continuous Wavelet Transform (CWT) instead of the Discrete Wavelet Transform (DWT) in Stage 2. Recall that DWT coefficients have half the size of the original data, while CWT coefficients have the same size as the original data, and thus have better resolution than the DWT coefficients. However, the CWT computational complexity is higher than that of the DWT.

The CWT-based experimental algorithm has the same parameter settings as those selected for the DWT case. Figure 49 and Figure 50 present one-hop detection and no-hop decision performances for SNR levels between -6

and 21dB when using a one-level DWT transform and the CWT for scales equal to 1, 5, and 9. Results show that one-hop detection performances obtained for the DWT and CWT (with scale equal to 5) are very similar, but that the CWT performance is much worse for scale equal to 1. The one-hop results may be explained by recalling that the CWT with scale equal to 1 was shown in Section IV.C to be not well suited to extracting the TCF phase discontinuities. Results also show that for the no-hop detection case, the CWT (with scale equal to 1) is significantly better for the range of SNR levels investigated than with other scales selected. Thus, overall the CWT with scale value equal to 5 may be best suited for the one-hop and no-hop detection problems under investigation.

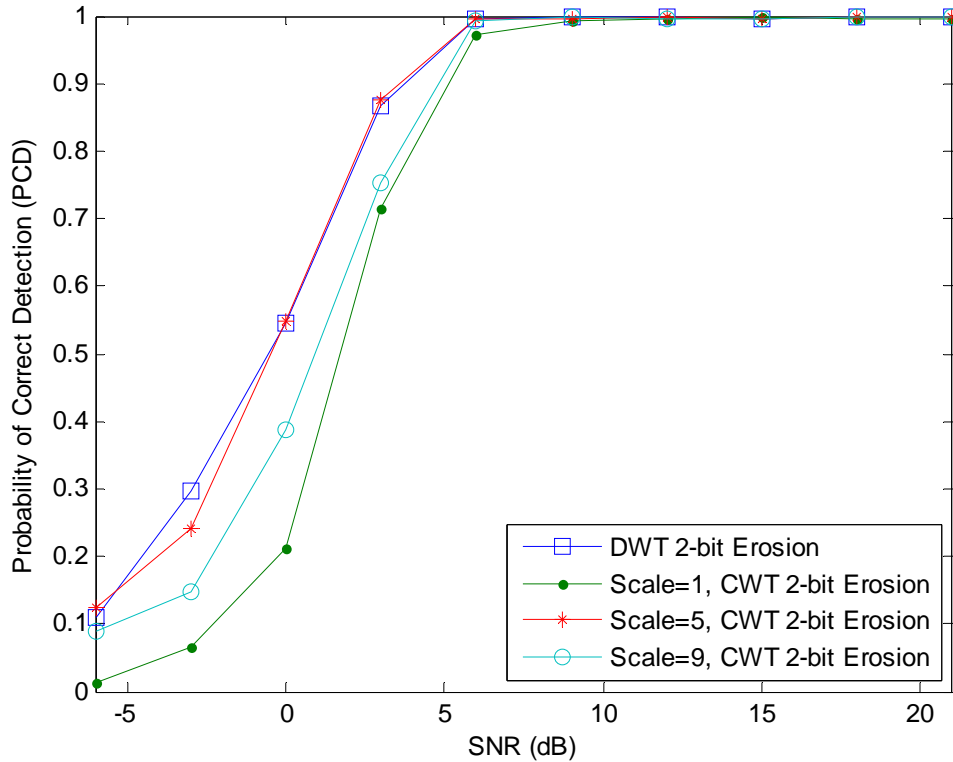


Figure 49. One-Hop Detection Performances for CWT at Different Scale Values and One-level DWT Transform, 2-bit Erosion Mask, 20% Detection Tolerance Level.

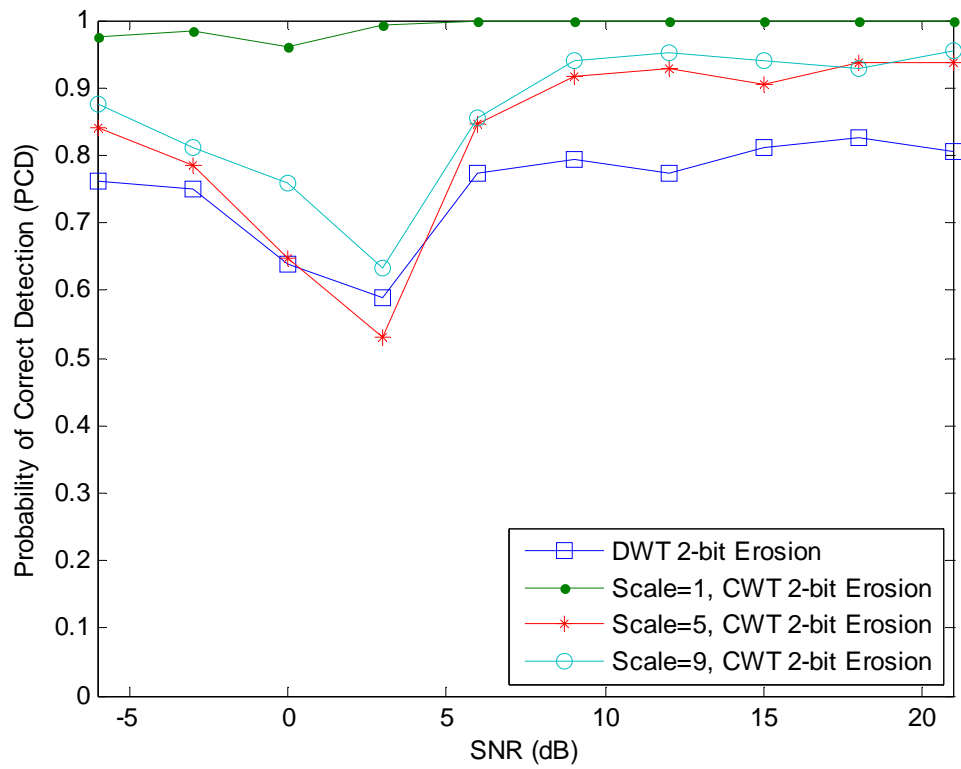


Figure 50. No-Hop Detection Performances for CWT at Different Scales and One-level DWT Transform, 2-bit Erosion Mask, 20% Detection Tolerance Level.

VII. CONCLUSIONS AND RECOMMENDATIONS

A. CONCLUSIONS

This thesis extended earlier work derived by Overdyk [3] and investigated the use of wavelet transform and image processing tools to estimate hopping times occurring in frequency hopping schemes, and investigated its robustness to additive white Gaussian noise distortions. The detection algorithm identifies frequency hopping time locations found in FH schemes from the information provided by the two-dimensional short-term signal temporal correlation function. Hopping time locations are shown by indentifying TCF phase discontinuities. The detection scheme has three main stages: 1. Derive the analytic version of the FH signal and compute the resulting TCF function; 2. Enhance discontinuities via the one-dimensional Wavelet transform; 3. Apply morphological image processing operations and the Hough transform to estimate hopping time locations.

Results show reliable detection performance may be obtained for SNR levels above 3 dB and good detection performance for SNR levels above 6dB for 5% to 20% detection accuracy

Simulations show that the erosion step improves the probability of correct detection (PCD) by 12% when the SNR level is equal to 3 dB. However, the erosion operation does not result in consistent significant improvement overall. Results also show that similar performance may be obtained both for DWT (scale $a=2$) and CWT (scale=5) implementations.

Results show that the basic one-hop detection scheme reaches 100% accuracy for 5% tolerance level and above when SNR level is above 6dB level. However, the no-hop decision scheme results in a 70% accuracy at 3dB, increasing to 90% and above only for high SNR levels. Results also show that adding the short-term variance tracking step at the beginning of the detecting

process boosts no-hop decision results to 100% at SNR levels above 6 dB without degrading the one-hop detection results.

Finally, basic FH and pulse-shaped FH signal types were investigated. Results show that lower detection performance is obtained when half sine pulse-shaping was applied to the symbols. This is to be expected, as pulse-shaping results in dampening the signal amplitude at both ends of a symbol, thereby making it harder to extract TCF phase discontinuities.

B. RECOMMENDATIONS

This thesis applied one-dimensional wavelet and two-dimensional image processing schemes to extract hopping time locations. The algorithm developed was successful in identifying hopping times. However, improvements in the detection performance could potentially be obtained by refining the scheme proposed in this work.

First, Basic FH and pulse-shaped FH signals were investigated. Results show that lower detection performances are obtained when half sine pulse-shaping is applied to the symbols. Thus, more sophisticated schemes may be needed to extract the smaller phase discontinuities in such scenarios.

Results also show the specific morphological erosion and dilation operations applied in this work do not improve resulting detection performance significantly, even though, they initially appeared to clean up the TCF phase information. Simulations showed that for low SNR levels the selected erosion operation could further erode fragmented line segments present in the image, and contribute to additional detection errors. A different set of morphological erosion/dilation operations which do not have this drawback would be needed to improve detection performance.

In Chapter III, we discussed a basic no-hop identification scheme which was based on short-term variance tracking of the basic TCF Phase expression for a specific lag value τ . We showed the scheme to be quite successful in

improving one-hop detection performance. However, further improvements may be obtained by tracking the TCF phase behavior for several lag values and combining the results.

The proposed scheme requires the user to select several parameters along the way; median filter lengths, wavelet type and length, morphological mask types and sizes. The results provided are the best that were obtained by selecting these parameters by trial and error when using the DWT implementation. These results indicate that the set of parameters selected for the DWT may not be the best for the CWT implementation, and further investigation is needed to determine whether the CWT could lead to better one-hop detection performance than reported here.

THIS PAGE INTENTIONALLY LEFT BLANK

LIST OF REFERENCES

- [1] M. Song; S. Wigginton, "Frequency Hopping Pattern Detection in Wireless Ad Hoc Networks," *2005 International Conference on Information Technology, Coding and Computing*, Vol. 2, 4-6 April 2005, pp. 633 – 638.
- [2] J. R. Hampton, "An Edge Detection Technique For Fine Acquisition In Frequency Hopping Radios," *1993 IEEE Communications Conference*, Vol.1, 11-14 Oct. 1993, pp. 198 – 202.
- [3] H. F. Overdyk, *Detection And Estimation of Frequency Hopping Signals Using Wavelet Transforms*, MSEE Thesis, Naval Postgraduate School, Sep. 1997.
- [4] B. Sklar, *Digital Communications Fundamentals and Applications*, Prentice Hall PTR, 2001, pp. 738-745
- [5] O. Rioul; M. Vetterli, "Wavelets and signal processing," *IEEE Signal Processing Magazine*, Vol. 8, Oct. 1991, pp.14 – 38.
- [6] M. Misit; Y. Misiti; G. Oppenheim; J.M. Poggi, "Wavelet Toolbox User's Guide", The MathWorks, Mar. 1996, pp. 1-5.
- [7] P.M. Bentley; J.T.E. McDonnell, "Wavelet transforms: an introduction," *IEEE Electronics & Communication Engineering Journal*, Vol. 6, Aug. 1994, pp.175 – 186.
- [8] R. Cristi, "Muti-Resolution Decomposition," *Unpublished Course Notes*, Naval Postgraduate School, Dec. 2007.
- [9] Y. Wang; J. Ostermann; Ya. Zhang, *Video Processing and Communications*, Prentice Hall, 2002, pp. 562-563.
- [10] R. Cristi, "The Elements of Image Analysis and Computer Vision," *Unpublished Course Notes*, Naval Postgraduate School, Dec. 2007.
- [11] R. Cristi, "Find Lines on an Image," *Unpublished Course Notes*, Naval Postgraduate School, Dec. 2007.
- [12] Wikipedia, "Hilbert transform," [Online] http://en.wikipedia.org/wiki/Hilbert_transform#Domain_of_definition, Aug 2008.
- [13] MATLAB Help Menu, "Find edges in grayscale image," The MathWorks, [Online] <http://www.mathworks.com>, Jan. 2007.

THIS PAGE INTENTIONALLY LEFT BLANK

INITIAL DISTRIBUTION LIST

1. Defense Technical Information Center
Kingman Rd., STE 0944
Ft. Belvoir, Virginia
2. Dudley Knox Library
Naval Postgraduate School
Monterey, California
3. Chairman, Code EC
Department of Electrical and Computer Engineering
Naval Postgraduate School
Monterey, California
4. Prof. Monique P. Fargues, Code EC/Fa
Naval Postgraduate School
Monterey, California
5. Prof. Roberto Cristi, Code EC/Cx
Naval Postgraduate School
Monterey, California